2022

Printing, Characterization, and Mechanical Testing of Additively Manufactured Refractory Metal Alloys

Brianna M. Sexton
Wright State University

PRINTING, CHARACTERIZATION, AND MECHANICAL TESTING OF ADDITIVELY MANUFACTURED REFRACTORY METAL ALLOYS

A Thesis submitted in partial fulfillment of the
requirements for the degree of
Master of Science in Mechanical Engineering

by

BRIANNA M. SEXTON

B.S.M.E., Wright State University, 2021

2022

Wright State University

WRIGHT STATE UNIVERSITY

GRADUATE SCHOOL

APRIL 27, 2022

I HEREBY RECOMMEND THAT THE THESIS PREPARED UNDER MY SUPERVISION BY Brianna M. Sexton ENTITLED Printing, characterization, and mechanical testing of additively manufactured refractory metal alloys BE ACCEPTED IN PARTIAL FULFILLMENT OF THE REQUIREMENTS FOR THE DEGREE OF Master of Science in Mechanical Engineering.

_____

Nathan Klingbeil, PhD.
Thesis Director

_____

Raghavan Srinivasan, Ph.D., P.E.
Chair, Department of Mechanical and Materials Engineering

Committee on Final Examination:

_____

Nathan Klingbeil, PhD.

_____

Ryan Kemnitz, PhD.

_____

Daniel Young, PhD.

_____

Barry Milligan, Ph.D.
Vice Provost for Academic Affairs
Dean of the Graduate School

ABSTRACT

Sexton, Brianna M. M.S.M.E., Department of Mechanical and Materials Engineering, Wright State University, 2022. Printing, characterization, and mechanical testing of additively manufactured refractory metal alloys.

Refractory metal alloys in the tungsten molybdenum rhenium ternary system were additively manufactured using laser power bed fusion. Four ternary alloys with varying concentrations of tungsten, molybdenum, and rhenium were manufactured and manufactured again with an addition of 1 wt% hafnium carbide. Samples were heat treated to heal cracks, reduce porosity, and reduce inhomogeneity. Material microstructure was characterized before and after heat treatment using microscopy, energy dispersive x-ray spectroscopy, and electron backscatter diffraction mapping. Mechanical testing was conducted on both three-point bend specimens and compression specimens, resulting in maximum bending strengths of 677.86 MPa, and maximum compression 0.2% yield strengths of 583.88 MPa for the strongest composition. The ternary alloy samples exhibited less porosity, less cracking, more refined grains, and higher strengths. The hafnium carbide doped samples exhibited more cracking and porosity, larger grains, and lower overall strengths.

TABLE OF CONTENTS

LIST OF FIGURES

LIST OF TABLES

I. INTRODUCTION

1.1 Refractory Metals

Refractory metals are a small group of materials which can maintain high strength at high temperatures and can withstand heavy wear without breaking down. They have high melting points and boiling points, good corrosion resistance, and BCC structure. The metals most commonly classified as refractory are tungsten, molybdenum, niobium, tantalum, rhenium, and sometimes hafnium [1]. Due to their exceptional heat resistance and mechanical properties, they are desirable for use in high-temperature applications such as the aerospace and automotive industries. There are several drawbacks to refractory metals but the most important may be the difficulty in manufacturing. Their high melting points and exceptional hardness, high strength, and brittleness all contribute to poor workability and necessitate expensive processing methods. Thus, it is desirable to find ways to produce parts using these materials more easily and in a less costly manner.

1.1.1 Tungsten

Tungsten has the highest melting point of all metals at 3422°C, and exemplary strength with a tensile yield strength of about 750 MPa [2]. As a refractory metal, tungsten remains strong even at highly elevated temperatures as well. Tungsten, like most refractory metals, possesses a body centered cubic (BCC) unit cell which makes dislocation motion more difficult than in face centered cubic metals. The difficulty in dislocation motion or plastic deformation leads to brittleness and gives rise to a ductile-

to-brittle transition at elevated temperatures. The ductile-to-brittle transition temperature (DBTT) marks the point where elevated temperature enables dislocation motion to occur more easily and the material behaves in a ductile fashion above this temperature. Depending on processing method, tungsten's DBTT is usually reported as between 400-600°C [3]. In most processing methods, the DBTT will be crossed several times, creating an unfavorable thermal gradient, and leading to embrittlement. Repeatedly crossing the DBTT results in persistent microcracking and internal stresses [4]. Tungsten is also one of the densest refractory metals at 19.3 g/cm^3. Its high density creates a limitation on the uses for tungsten, particularly for aerospace applications where weight of components is important. For many applications where lightweight materials are desired, tungsten's high strength does not offset the impact of the extra weight.

Alloying tungsten with other materials with lower densities and DBTTs can have several benefits, such as increased mechanical strength, lowered DBTT, and lower overall alloy weight [5, 6]. Lowering the DBTT lowers the number of cracks, which also results in a stronger part. Additionally, the lower DBTT could influence the fracture mode from brittle to ductile [7]. Although tungsten is strong at both room temperature and elevated temperatures, a lowered DBTT is vital in order to reduce its brittleness and the detrimental effects of cracking. Alloying can also help refine grain sizes during processing by raising the recrystallization temperature of the alloy [8]. Smaller grains generally result in higher strength because of the Hall-Petch relationship [9].

As with most metals, oxidation of tungsten leads to embrittlement. Oxidation causes grain boundary impurities and nanopores that lead to more cracking [6, 10]. Seeing as how tungsten's high DBTT already makes it susceptible to cracking, this is a major problem when considering manufacturing of tungsten. Low oxygen content is important for strong, fully dense tungsten parts [8, 11].

1.1.2 Molybdenum

Molybdenum is less dense than tungsten at 10.22 g/cm^3 but is also weaker, with a 400 MPa yield strength and exhibits a lower melting point of 2622°C [12]. The DBTT of molybdenum is closer to room temperature, which means that it is less prone to cracking and can be more ductile at lower temperatures when compared to tungsten. Still, pure molybdenum is a brittle material because of its BCC structure, and it oxidizes easily at high temperatures [13, 14], so it is not ideal to use on its own without alloying. It is also known that obtaining homogeneous molybdenum samples can be difficult without high-temperature annealing, which results in large grain sizes, and that alloying can help refine the grains again [15, 16]. Depending on the need driving alloy creation, a tungsten-heavy or molybdenum-heavy alloy could trade off resulting weight and grain refinement with mechanical strength and ductility.

Like tungsten, oxidation easily embrittles molybdenum. However, it is more of a concern for this metal because of its unusually weak grain boundaries [17]. Any impurities or gas pores segregated to the grain boundaries will render molybdenum

samples weak [18–20]. Pure molybdenum tends to segregate oxygen, nitrogen, and other elements at the grain boundaries, but even samples with little to no grain boundary segregation will still have brittle intergranular fracture [10, 21–23].

1.1.3 Rhenium

Rhenium is more dense than both tungsten and molybdenum, at 21.04 g/cm^3, and weaker than the other two, with a yield strength of 290 MPa. It also has a high melting point, at 3185°C. Unlike the majority of the refractory metals, rhenium has HCP structure, which is typically considered a more brittle structure due to the lower symmetry [24]. Despite these apparent downsides, rhenium is a useful alloying element because it can help improve the properties of the other refractory metals, particularly the ductility and strength of tungsten and molybdenum [25–29]. By alloying with tungsten or molybdenum, the alloy's DBTT can also be reduced to ease thermomechanical processing and reduce cracking [30–32]. When alloying with molybdenum, rhenium has an observed softening effect up to about 20 wt%, at which point the performance improves greatly [33]. Generally, alloying any refractory metal with rhenium will have a beneficial effect on the alloying metal's properties. It is worth noting that rhenium is more expensive than tungsten or molybdenum, so while its inclusion is useful, it is also desirable to lower costs by finding the minimum amount of it that can be added while still reaping the benefits.

1.1.4 Hafnium Carbide

There is some interest in improving base metal properties through the inclusion of nanoparticle additives, which can refine grain size and improve strength [34–36]. Hafnium carbide has a high melting point of 3900°C and a median density of 12.2 g/cm^3. Like tungsten and molybdenum, it has BCC structure. It has been proposed that hafnium carbide inclusion in tungsten and molybdenum alloys may provide improved tensile strength instead of previously supposed solute weakening and has been shown to refine grains [37, 38].

Carbides are known to help increase strength of molybdenum grain boundaries and shift fracture mode from intergranular to transgranular [39, 40]. Hafnium is also a good alloying element for increasing the strength of weak grain boundaries. Adding hafnium to molybdenum also helped influence the fracture mode from intergranular to transgranular without creating solutes [41]. Hafnium is also considered one of the better elements to alloy with molybdenum-rhenium alloys, because it can increase high temperature strength without totally embrittling the material [42]. Overall, when considering potential nanoparticle additives for the W-Mo-Re alloys, hafnium carbide was the strongest contender.

1.2 Additive Manufacturing

Additive manufacturing (AM), or 3D printing, is the process of creating materials using a layer-by-layer building method. AM was first invented in the 1980s and has been increasingly popular in the public eye over the past decades. There are several different

types, each of which is best suited for certain materials. For example, material extrusion involves laying down softened layers of extruded plastic filaments, while selective laser melting uses a laser to melt layers of metal powders. Part of the reason for the growing interest in AM is its innovation in design freedom and potential savings on material cost. Designs which are impossible to make through traditional manufacturing are possible with AM, and less material is used overall because of the lack of need to start with blocks or sheets and cut material away to manufacture the desired geometry. Typically, the only materials used are those that make up the part itself. Even with designs that require support structures because of overhangs or steep angles, the supports are often easily removed by being snapped off or dissolved. Unused materials are also often recyclable in AM. For example, in powder-based processes that require a full bed of powder regardless of how small the printed part is, any excess powder can be recycled and used in the next print.

As with any new technology, additive manufacturing presents its own unique challenges in practical use. For example, layer adhesion is crucial to obtaining solid parts. If the layers do not bond well to one another, the resulting parts will have poor cohesion, low density, and low strengths. Also, as previously stated, any parts that have overhangs or angles steeper than 45° need a support structure to hold shape well during the printing process. Because parts are either soft or briefly molten during printing, these geometries would fall apart without extra vertical support. Lastly, as-printed surface finishes tend to be rough, and in some AM methods the parts are still soft when removed from the printer.

As such, it is common to surface polish or treat parts before use. Additionally, certain finer details such as threaded bolt holes may need to be machined after the fact, which adds both time and cost to the process.

1.2.1 Laser Powder Bed Fusion

Laser powder bed fusion (LPBF) is the metal AM technique which creates materials by using a laser to melt layers of fine metal powders. In LPBF, a chamber is filled with powder stock, which is wiped onto a build plate by a rubber or metal roller or wiper. Once the build plate has been coated with powder, the desired layer's geometry is melted by the laser. The build plate then lowers down, the powder chamber rises, and powder is wiped onto the build plate again so that the laser can melt the next layer. Because this process involves high temperatures and molten metals, printing is conducted in an inert gas environment. The most common shield gas for LPBF is argon, although different atmospheres such as hydrogen-argon mixtures and nitrogen have been used successfully as well [43]. The quality of the resultant parts is influenced by both the powder quality and the combination of printing parameters used.

Powder quality refers to whether the powder has been spheroidized, the average particle diameter of spherical powders, and the number of prints that a given batch of powder has been used in. If powder is uniform and spherical, it will wipe across the powder bed and partially printed parts more smoothly and more effectively absorb laser power during melting [11, 44]. Conversely, if the powder is non-uniform and non-

spherical, the wiping can be more erratic, and parts may not print as smoothly. While leftover powder can be recycled into subsequent prints, some studies show that repeated recycling can lead to increased average powder diameter and less uniformly spherical particles. These instances may lead to increased number of defects in printed parts and a decrease in material strength. The exact mechanisms behind this and effects on printed parts are debated, as conflicting results have been reported in the literature, but the distinction between fresh and recycled powder is worth noting [45–47].

Printing parameters are settings that can be changed per print and should be tailored to material and part shape. These include the laser power, laser speed, powder layer thickness, print pattern or scan strategy, shield gas, and laser hatch spacing.

Among all these printing parameters, the design of the part must still be taken into account. Extremely thin pieces may be weak and fail to print. Large areas may become overwhelmed with heat and result in an over-melted, porous part. Certain geometries will need support structures. These kinds of considerations must be taken no matter what printing parameters are selected. Regardless of how fine-tuned a parameter set, care must still be put into part geometry to ensure ideal results.

Energy density (E_V) is the amount of energy put into a print and is calculated as a relationship between laser power (P), laser speed (V), hatch spacing (H), and layer height (L), and is represented as

$$E_V = \frac{P}{V * H * L} \quad (1)$$

LPBF prints need an ideal E_V to have a favorable result [11], [48]–[51]. If the E_V is too low, the powder will not be fully melted, and parts will have pervasive lack of fusion porosity and low density. However, if it is too high, then samples will be overheated and unstable, which also results in keyhole porosity. In either case, the part may simply fall apart before the print finishes or may complete printing but have low strength. Doing parameter studies with new alloys to tweak the E_V and find its ideal range is subsequently vital for LPBF.

During LPBF, powder is heated to its melting point and then rapidly cools every layer. Because of this, thermal gradients are created, and printed samples can have micro-cracking due to internal stresses or balling defects due to high surface tension and viscosity [52, 53]. Tungsten, for example, is infamously well-known for cracking during additive manufacturing [10, 54]. Work has been done, with limited success, to suppress the micro-cracks either through alloying or the use of pre-heated build plates [40, 55].

1.3 Analysis

Oxidation is a common concern for AM methods, especially ones like LPBF where materials are melted and then solidified. Oxygen impurities can weaken grain boundaries and reduce the overall strength of the part, as well as affect the atomic chemistry of a printed alloy.

Three-point bend (3PB) tests are tests in which a straight, rectangular piece of material is bent, either to a maximum angle or to failure, with three points of contact. Samples are set on two supporting points and are pressed down on from above by a third point in the center. The distance between the center points of the bottom two supports is called the span. Samples need to be a little longer than the desired span so that they can sit securely on the fixture even if they begin to bend significantly. The span, sample cross-sectional area, distance displaced, and maximum applied force can all be used to calculate the maximum bending stress.

$$\sigma = \frac{3 * F * L}{4 * w * t^2}, \tag{2}$$

where F is the force, L is the bend fixture span between the bottom points, w is the sample width, and t is the sample thickness. The value of σ at failure corresponds to the bending strength of the specimen.

Compression tests are tests in which some sample with known dimensions, with flexibility regarding sample geometry, is placed between two platens and compressed until failure at a given strain rate. The strain rate is based on the height of the specimen, rather than a set independent value. Compression tests are useful to determine if samples will simply crumble apart or if they will deform under pressure – and if so, how the deformation will look. The resulting force and displacement data, along with the sample dimensions, can be used to calculate engineering stress and strain as

$$\varepsilon = \frac{\Delta l}{l} \tag{3}$$

and

$$\sigma = \frac{F}{A}, \tag{4}$$

where ε is the strain, σ is the stress, l is the height, Δl is the change in height caused by the displacement, F is the applied force, and A is the cross-sectional area of the sample.

From the engineering stress and strain plots, the Young's modulus (or modulus of elasticity) and 0.2% yield strength can be found. In a stress vs strain plot, there will be a straight section of elastic deformation before the plot curves as plastic deformation begins. The slope of the straight line is the Young's modulus. Using this slope, a parallel line may be plotted with an added offset of 0.002 strain. The intersection of this straight line and the plotted stress and strain graph will be the 0.2% yield strength. An example of this is shown in Figure 1.

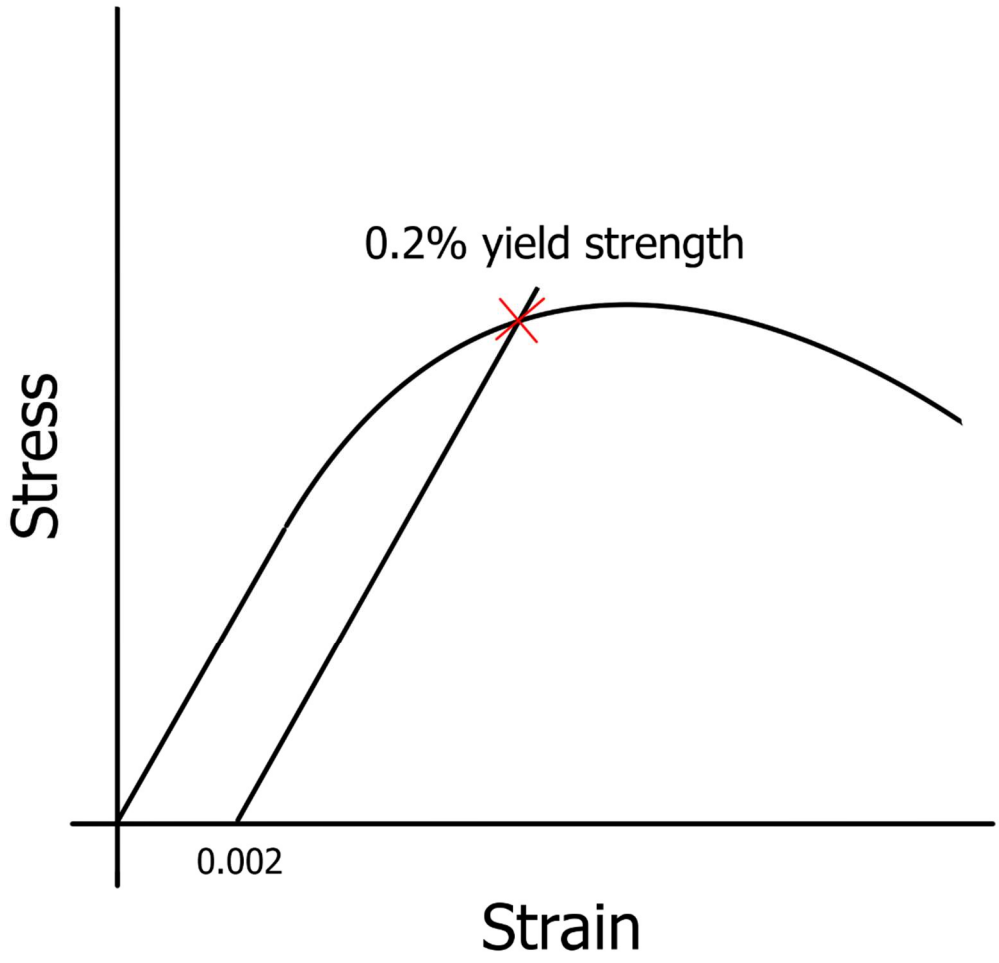

Figure 1: Yield strength measurement diagram

Grain orientation and size are important factors to consider when analyzing printed parts. Impurities like oxygen or carbon at the grain boundaries (GBs) can make GBs weaker, resulting in easier intergranular fracture and an overall weaker specimen [7]. While alloy strength depends on a number of factors, it is also generally noted that

refined grains lead to stronger and more ductile materials than those with large grains [56, 57]. This is because fractures must break through more GBs when the grains are smaller. Additionally, the GB structure can influence the brittleness of a material. It has been found that increasing the number of strong low-sigma GBs and reducing the number of weak random GBs can reduce brittleness [58].

Heat treatments are a form of post-processing for samples created by additive manufacturing. By their nature, additive processes often result in parts with internal stresses, microcracking, and porosity. This is nearly impossible to entirely suppress using alloying, pre-heating, or specific combinations of printing parameters alone. Because of this, samples will often be brought to elevated temperatures for extended periods of time with the intention of improving the as-printed material. Heat treatments can help improve ductility, encourage diffusion in poorly mixed alloys, increase strength, and seal thin cracks and small pores [28, 59].

SEMs work by creating a vacuum inside the chamber, and then shooting a beam of electrons at a sample. The intensity of the detected electron response is interpreted as depths, with different heights displayed as different brightness levels, which creates the image. These microscopes can take highly magnified and extremely detailed pictures. Additionally, when pairing an SEM with other detectors, several microscopy methods can be employed to help analyze and classify materials.

Energy dispersive spectroscopy (EDS) is a surface analysis tool which enables users to use an SEM to scan a material and obtain an approximation of the chemical composition of a sample. EDS works by exciting samples and obtaining the electron emission spectra. Because each element has a unique spectrum, the software is able to assign elemental identities to each emission line. It is often used in identifying unknown materials. EDS is also able to offer an estimation of the ratio of materials present, in percentages. However, because EDS scans have only shallow penetration into a sample's surface, and because many elements have similar or partially overlapping emission spectra, the results are imperfect. They are best used as an estimation, rather than a quantitative report.

Electron backscatter diffraction (EBSD) is another SEM method which can excite electrons to detect crystallographic information and detect grains. For EBSD, samples are tilted at a 70° angle. EBSD is able to detect the size of sample grains, as well as their crystallographic directions (110, 101, etc.) and grain misorientation angles. Samples with grain misorientation angles lower than 15° are said to have grains with low angle grain boundaries (LAGBs), which often hints at the presence of dislocations that can affect the properties. Samples with high angle grain boundaries typically do not depend on dislocations [60]. The method is also used to report on the crystalline structure of a sample. It can detect whether a sample is body-centered cubic (BCC), face-centered cubic (FCC), or something else, and can give an estimated percentage of each if samples are a

mixture of two or more. In order to properly carry out EBSD mapping, samples must be polished to a mirror finish and then etched.

1.3 Research Questions

Refractory metal alloys are of great interest currently for many applications, but many combinations have little to no reported data in the literature. One alloy space with little reported data is the W-Mo-Re area. In order to survey the area, varying amounts of each of the three metals were selected. First, two alloys composed of primarily tungsten were selected with 10 and 20 wt% rhenium respectively. Then, alloys composed of primarily molybdenum were selected by trading off the amounts of tungsten and molybdenum. Thus, the alloy 70W-20Mo-10Re also led to 20W-70Mo-10Re. Likewise, selecting the alloy 50W-30Mo-20Re led to 30W-50Mo-20Re. With this group of alloys, both tungsten-heavy and molybdenum-heavy materials were studied with varying amounts of rhenium, both above and below the rhenium softening threshold in molybdenum.

The specific weight percentages of alloys were selected based on the ternary phase diagram of the tungsten molybdenum rhenium system, as plotted by the Thermo-Calc software. Compositions were selected to remain within the BCC solid solution phase without including any sigma or HCP phases. The phase diagram is presented in Figure 2 below.

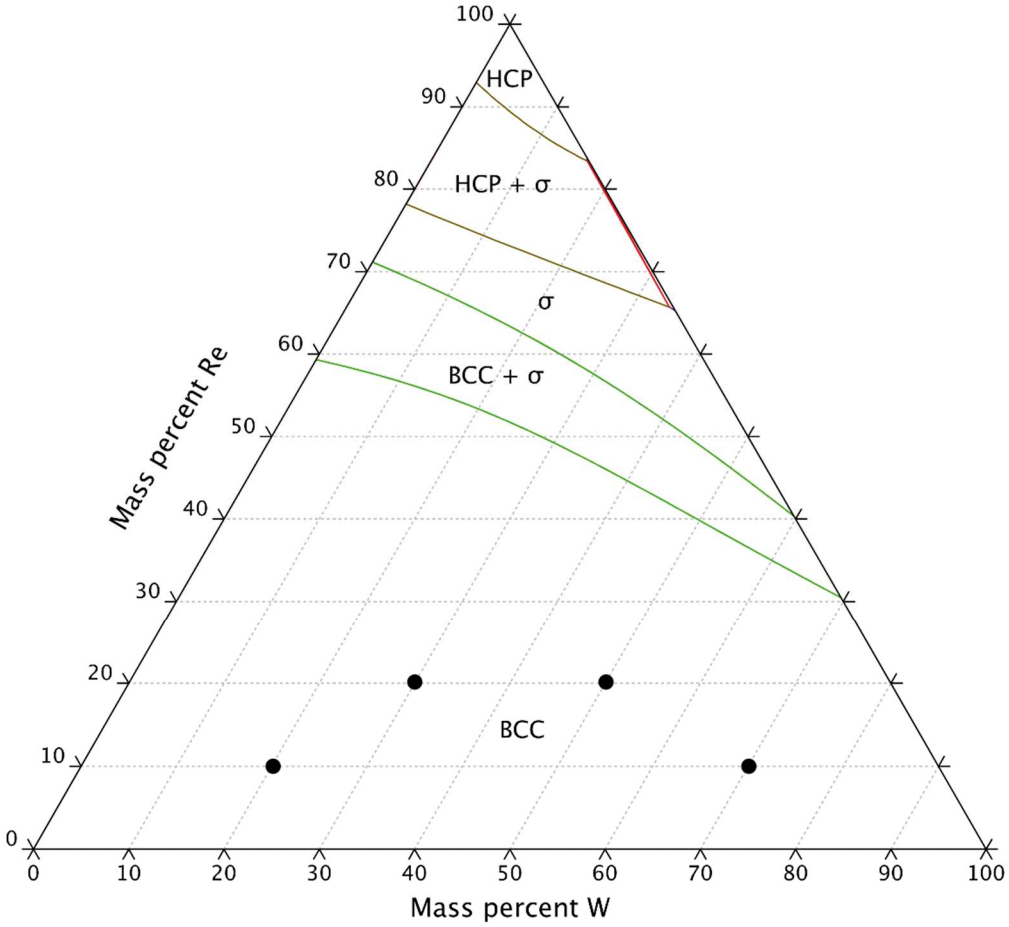

Figure 2: W-Mo-Re phase diagram (Thermo-Calc)

Additionally, improvement of printed metal alloys by several different means is of great interest to those looking to employ the use of these materials. One such potential method is by use of additives such as nanoparticles, to refine grain sizes and improve alloy strength. For this research, 1 wt% of the nanoparticle hafnium carbide was added to each of the four base alloys, creating a total of eight alloys included in this study.

The questions that this research addresses are as follows:

1. Can LPBF be used to successfully print strong refractory metal alloys?
2. How does the W-Mo-Re ternary space behave as the composition is adjusted with respect to each element?
3. How does the addition of a nanoparticle such as HfC affect the overall performance of the alloy?

1.4 Methodology

Four base alloys with varying amounts of tungsten, molybdenum, and rhenium were printed using LPBF, and then reprinted with an addition of 1 wt% hafnium carbide. Samples were sent out for a 1600°C heat treatment, and the microstructure of heat-treated and un-heat-treated samples was analyzed using SEMs and optical microscopy. Three-point bend tests and compression tests were carried out on heat-treated samples. The data was used to calculate total elongation, yield strength, and the Young's modulus for each alloy.

1.5 Contributions

This thesis classifies a largely un-studied alloy area, using a new and rapidly growing technology for the preparation method. While similar studies with other materials have been carried out, none of the data presented in this thesis can currently be found in the literature. Overall, this thesis accomplishes three things:

1. Characterizes microstructure of a ternary space previously unstudied in metal additive manufacturing.

2. Reports the strengths of brand-new materials not found in the literature.
3. Discusses the use of nanoparticles in unique additively manufactured refractory metal alloys.

Not only does this work provide the items listed above, but it also lays the groundwork for future research in the field and offers data for comparison for further studies.

II. METHODOLOGY

2.1 Printing

The tungsten powder used in this research was spherical, with an average particle diameter of 25μm, purchased from TEKMAT. The molybdenum powder was also spherical, with an average diameter of 45μm, from TEKMAT. The rhenium powder was non-spherical sieved with a 635 mesh, purchased from Rhenium Alloys, Inc. Lastly, the hafnium carbine nanoparticles were 800 nm, purchased from US Research Nanomaterials, Inc. The powders were measured out by weight percent (wt%) and then mixed for two minutes in a DAC 250.1 FVZ-K FlackTek, Inc. SpeedMixer before being loaded into the printer.

Samples were printed using a Concept Laser Mlab Cusing 200R printer shown below in Figure 3. They were printed in a vertical orientation onto removable pucks inlaid inside of a steel build plate, shown below in Figure 4. The W-Mo-Re alloys were printed on copper pucks. However, early layers of the W-Mo-Re-HfC alloys had issues

with delamination and failed prints on the copper pucks, and so were printed on molybdenum pucks instead for better adhesion. The samples were printed with a nitrogen shield gas. The laser power was P = 200W, layer thickness was L = 20μm, hatch spacing was H = 50μm, and laser scan speed was V = 400mm/s. This set of parameters was chosen because preliminary prints of different parameters showed that this combination was ideal for printing tungsten molybdenum rhenium alloys. Once it was proven effective for one print, it was held constant for all eight alloys. Plugging the above information into Equation 1 results in an energy density of E_V = 400 J/mm^3. Samples were cut off the pucks with wire electrical discharge machining (EDM).

Figure 3: Concept Laser Mlab printer

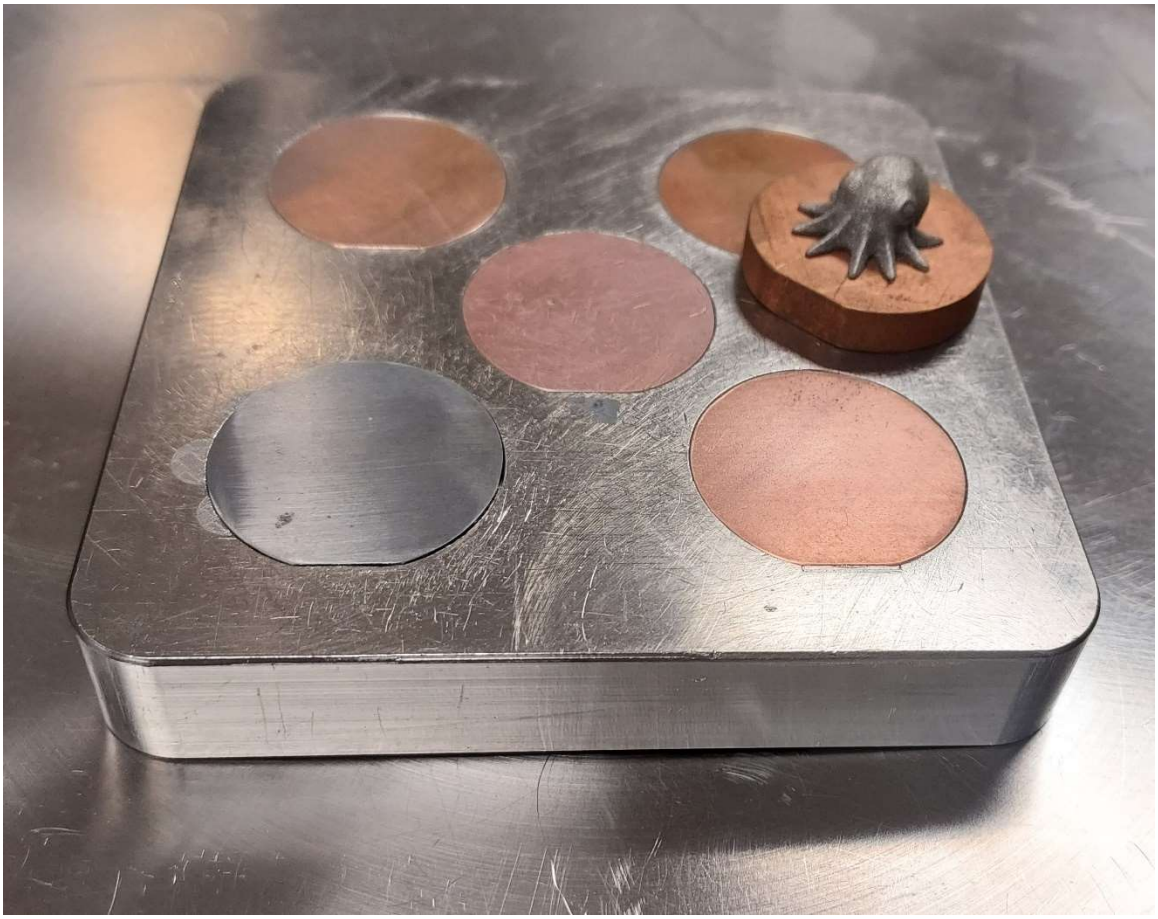

Figure 4: Build plate modified for removable pucks, with copper and molybdenum pucks loaded

Because identical prints with eight different alloys were carried out, samples were labeled to keep them distinguishable. The labeling convention used for this study was according to tungsten content, such that a sample with 20 wt% tungsten was labeled 2. Because the same alloys were printed with the addition of 1 wt% hafnium carbide, the alloys with the additive were labeled with a +, such that the alloy with 20 wt% tungsten

that contained hafnium carbine was labeled 2+. Complete alloy compositions for all eight materials are listed in Table 1.

Table 1: Sample Labeling Conventions

Label	Composition
2	20W-70Mo-10Re
2+	20W-70Mo-10Re-1HfC
3	30W-50Mo-20Re
3+	30W-50Mo-20Re-1HfC
5	50W-30Mo-20Re
5+	50W-30Mo-20Re-1HfC
7	70W-20Mo-10Re
7+	70W-20Mo-10Re-1HfC

There were two geometries of sample sets printed: cylinders for compressive tests, and rectangular bars for three-point bend tests. The compressive samples were printed with a height of 9.5 mm and a diameter of 6.25 mm. The micro three-point bend fixture had a minimum span of 4 mm, so the bars were also printed with a height of 9.5 mm to keep the prints thermally uniform and to supply extra length for the samples to sit securely on the three-point bend fixture. Their cross-section was 2 mm by 4 mm. They are shown below in Figure 5.

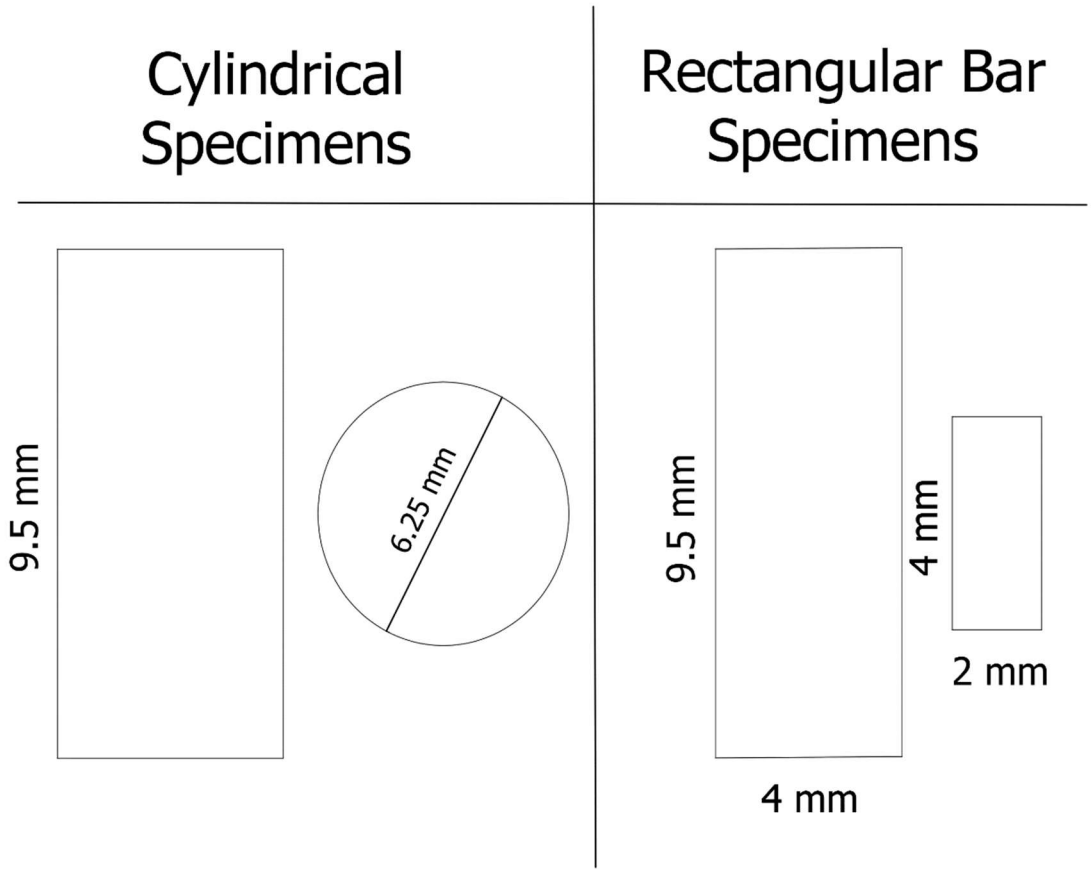

Figure 5: Printed specimen dimensions

2.2 Sample Preparation

After being cut off the pucks, the samples were sent for heat treatment. The samples were heated at 2200°C for 6 hours at Rhenium Alloys, Inc. Heat treatments are useful for parts made by LPBF because they can help close cracks and encourage diffusion of materials that may not have mixed completely during the printing process. Heat treatments will often result in enlarged grain sizes, but not so drastically that the pros do not still outweigh the cons. Because tungsten and molybdenum are both prone to

cracking during AM processes, heat treatments are almost always necessary for alloys containing substantial percentages of either. Additionally, the different particle sizes and melting points of all three main materials lend themselves to poor mixing. As such, the heat treatment was also vital for homogeneity, which leads to stronger parts.

The samples' rougher surface finish, characteristic of LPBF, was removed using a Buehler EcoMet 300 grinder-polisher. A 240-grit paper was used to remove the bulk of the rough surface from the bend specimens' two largest faces, shown in Figure 6, where force would be applied. Meanwhile the cylinders, shown in Figure 7, were ground with finer 400 grit papers. The lower rate of material removal was useful in ensuring that the parts remained rounded, without flat areas along the sides. For both the bend and compression specimens, grinding removed surface defects that could lead to potential crack propagation sites and skew failure load results.

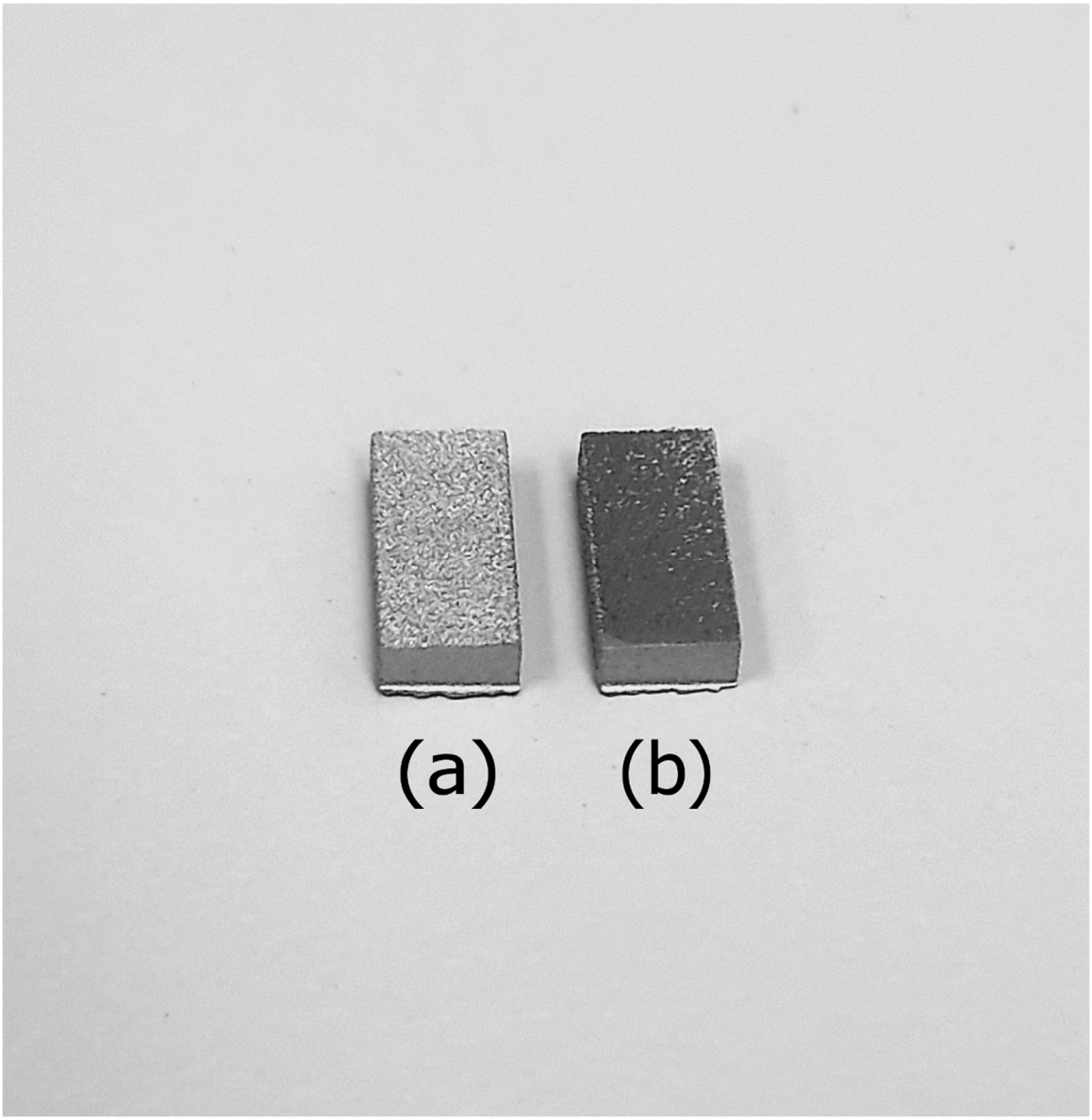

Figure 6: An (a) un-ground and (b) ground three-point bend specimen

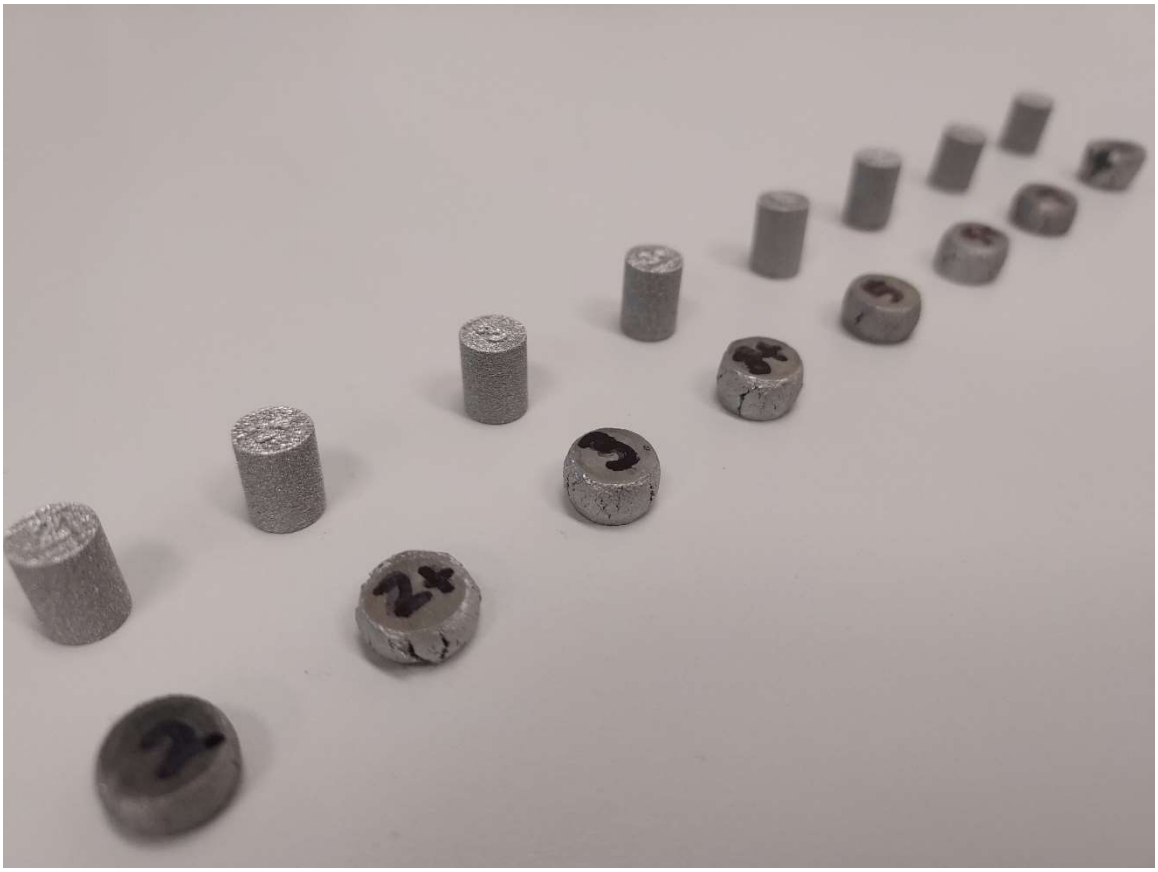

Figure 7: Compression specimens before and after crushing

2.3 Testing

Three-point bend testing was done on an MTS Acumen electric load frame equipped with an MTS micro three-point bend fixture. Three tests were done per alloy and averaged for the final result. The micro three-point bend fixture was set to its lowest setting, with a span of 4 mm. Tests were run until failure with a displacement of 0.01 mm/s. Failure for these tests was defined as the specimen broke far enough that it was unable to sustain load. In most cases, this meant that the samples broke into two pieces. The load frame and three-point bend fixture are shown below in Figure 8.

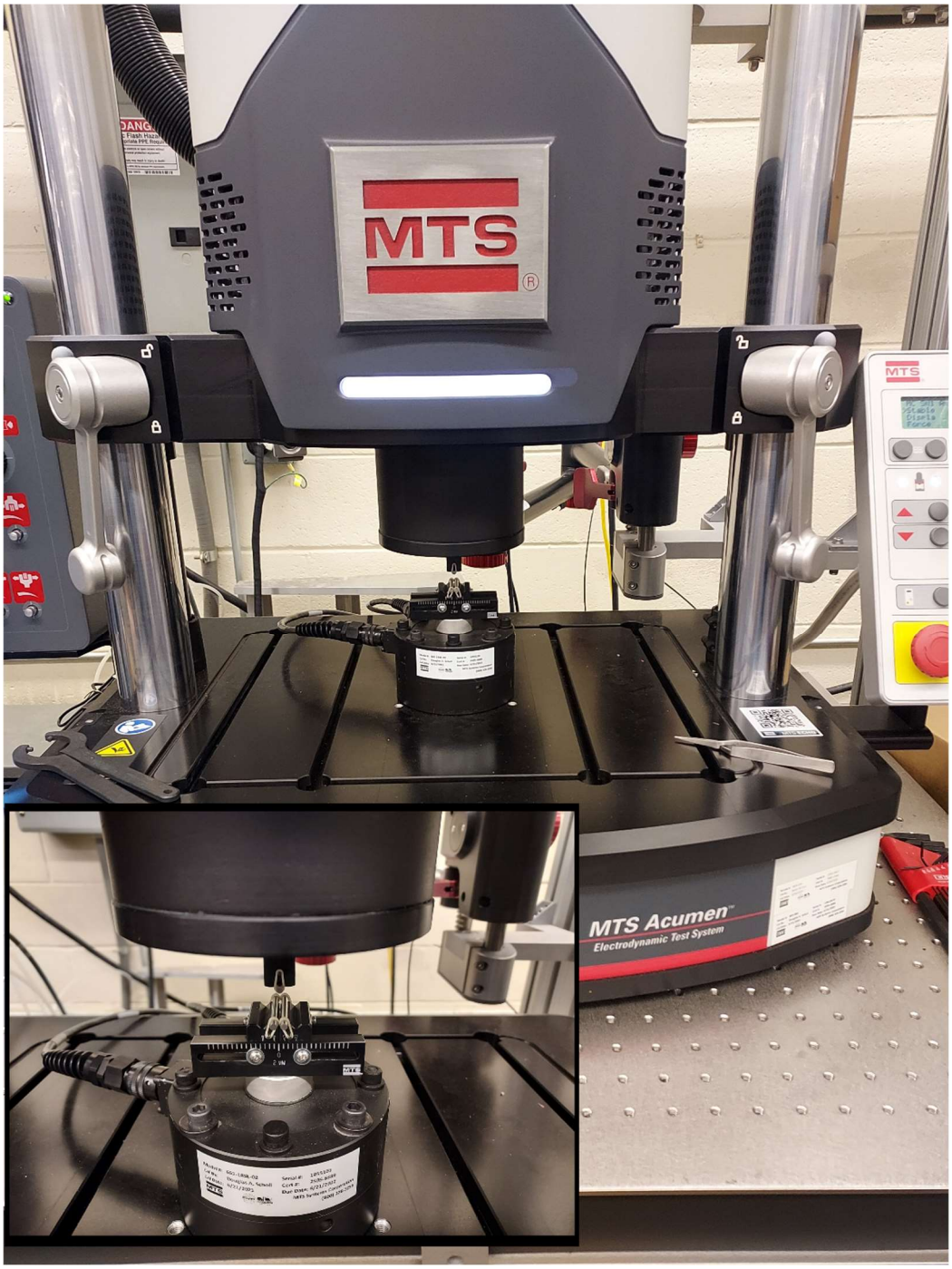

Figure 8: MTS Acumen load frame; MTS micro three-point bend fixture

Compression tests were carried out on a 110-kip MTS load frame. One sample was crushed per alloy, with a displacement rate based on the height of the sample, to a maximum endpoint of 50% engineering strain. The load frame is pictured below in Figure 9.

Figure 9: MTS 110-kip load frame for compression

2.4 Analysis

Fracture surfaces of broken three-point bend pieces were imaged in a TESCAN MIRA3 SEM. Images were taken at a working distance (WD) of 10mm, with view fields of 1000μm, 500μm, and 250μm. The beam intensity and high voltage (HV) were both set to 10W for imaging. The fracture surfaces showed grain size and in what fracture mode the specimens failed. Transgranular fracture is failure which passes through multiple grains, while intergranular fracture is failure which travels along the grain boundaries. Intergranular fracture is typically brittle and can be caused by weak grain boundaries [7]. Transgranular fracture can be favorable because of the indication that grain boundaries have been strengthened. Fracture surfaces can also show if there are any notable impurities such as oxides along the inner surfaces and can show if there was any ductility in the sample.

Broken pieces of bend specimens were mounted onto carbon pucks using a MetLab METPRESS A automatic mounting press, as shown in Figure 10. Samples were ground to near-mirror finish using the following grit papers: 240, 320, 400, 600, 800, 1200. Afterwards, they were polished using 9μm, 3μm, and 1μm MetaDi Supreme polycrystalline diamond suspension.

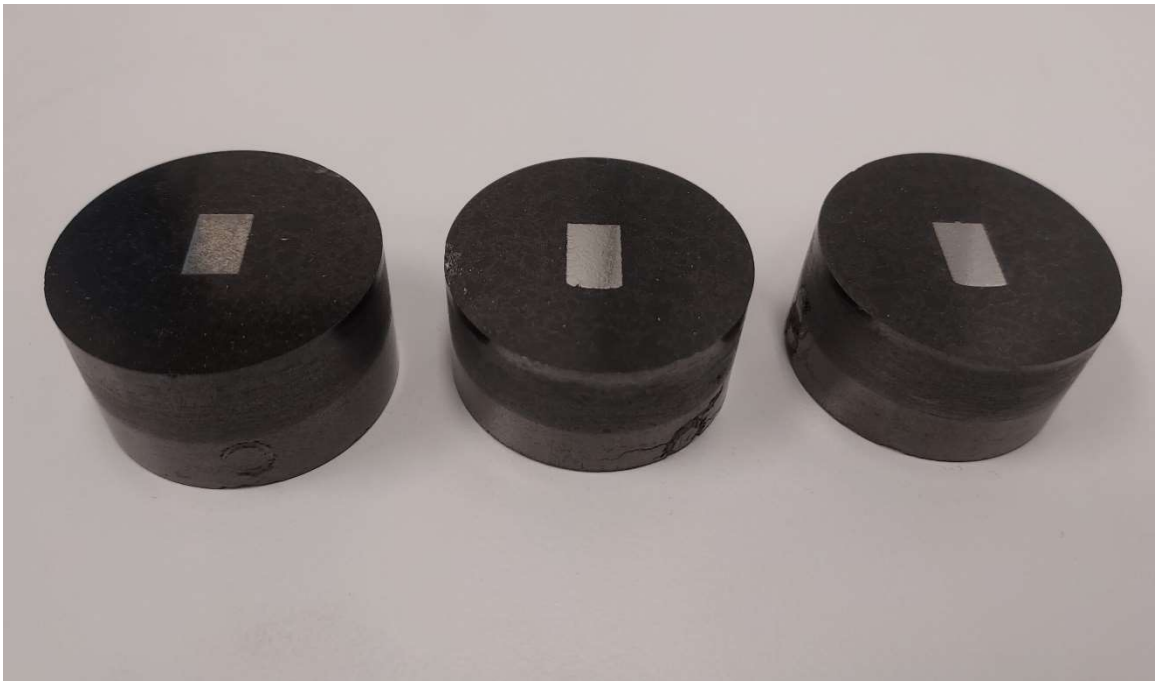

Figure 10: Pucked samples for microscopy

Polished pucks of both the heat treated and un-heat-treated samples were also analyzed with optical microscopy, using a ZEISS inverted microscope. Images of the surfaces were taken, and the percent porosity was measured using ZEISS ZEN core software. After surface analysis, they were etched using 20% hydrogen peroxide and rinsed with isopropyl alcohol. Etched pucks were then imaged again to see the size, shape, and orientation of the grains.

SEM images of the heat-treated samples to estimate grain size of the heat-treated samples. The method follows the standard, such that three lines are drawn across an image and the number of grains that it passes through are tallied up. A line passing straight through a grain was counted as 1 grain, while a line glancing through the border

of a grain was counted as 0.5 grains, and a line passing through a cluster of grain borders was counted as 2 grains. Images of the etched samples were used with high contrast settings in order to more accurately count the grains. An example of the method is shown below in Figure 17.

EDAX software was paired with the SEM to take EDS maps of polished pucks and EBSD maps of etched samples. These helped determine resulting elemental composition, grain size, and grain orientation. Because of the varying melting points and particle sizes, there is always the possibility of some percentage of each material boiling off during melting, or certain areas having concentrated amounts of one element over another. EDS scans are therefore a good qualitative self-check, because they can estimate the composition percentage per material. The EDAX software lists different areas with different alloy compositions as separate phases, not to be confused with physical phases such as solid solution BCC, FCC, etc. The software is sensitive so that different phases may differ by small percentages. The EBSD scans provided a more accurate grain size analysis than the optical observation method, and also reported on the grain orientations and crystal structure of the samples. The SEM WD was once again 10 mm, and maps were taken with 1000 mm view fields. However, the beam voltage was set to 15W for EDS mapping, and 18W for EBSD mapping.

III. RESULTS AND ANALYSIS

3.1 Top Surfaces

The top surfaces of the samples were analyzed in an SEM. They were imaged with 1 mm view fields, and examined for surface cracks, porosity, and weld track consistency. The results are shown below in Figure 11. Samples in the lefthand column are the base alloys, while samples in the righthand column contain hafnium carbide. They increase with increasing tungsten content as per the labeling system, from 2 to 7.

Each of the samples display some level of microcracking, which is typical with additively manufactured tungsten and molybdenum. Because all the samples exhibit fine cracking, it is not an immediate concern. Many times, the cracking will not be present deeper into the sample below the surface, and the heat treatment should heal the majority of fine cracking. Porosity is relatively low. It is more prevalent in the hafnium carbide samples, namely the 2+ and 5+ samples. Aside from areas interrupted by pores or cracks, the weld tracks are consistent across the board.

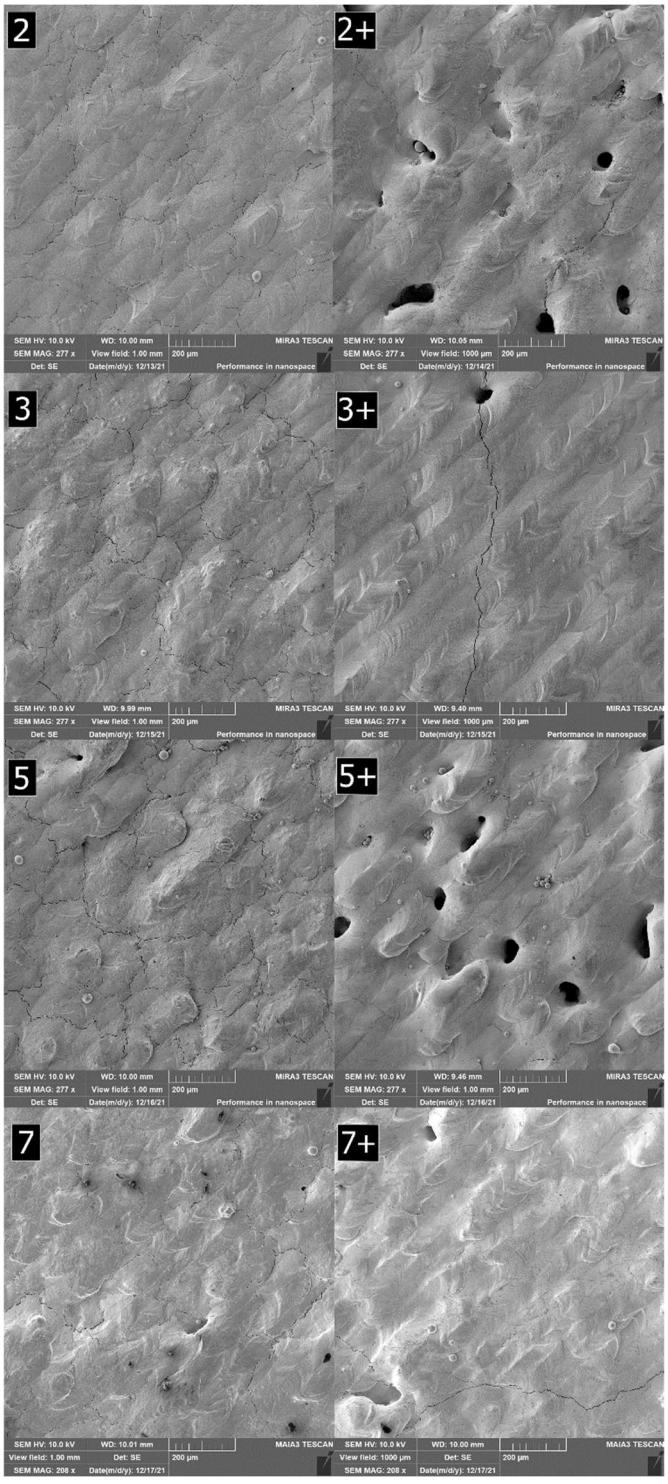

Figure 11: Printed top surfaces

3.2 Pre-Heat Treatment Microstructure

Because previous studies with similar materials displayed underwhelming strength in the as-printed state, no un-heat-treated samples were tested for strength in this research. However, one sample of each was held back from the heat treatment batch in order to study the microstructure and gauge the amount of improvement before and after.

Samples were mounted in carbon pucks and ground into to see the microstructure beneath the surface, which can often differ significantly from the top surfaces. Figure 12 shows the polished surfaces of the samples before heat treatment.

In all of the un-heat-treated samples, porosity is generally low, and there is no notable cracking. On the contrary, the hafnium carbide samples display more notable porosity, and they all had pervasive side-cracking on the samples, which was deep enough to still be apparent on the polished surfaces. Additionally, the samples display clear lack of dispersion. The lighter spots are concentrations of metals, showing that the materials did not mix completely in the as-printed state.

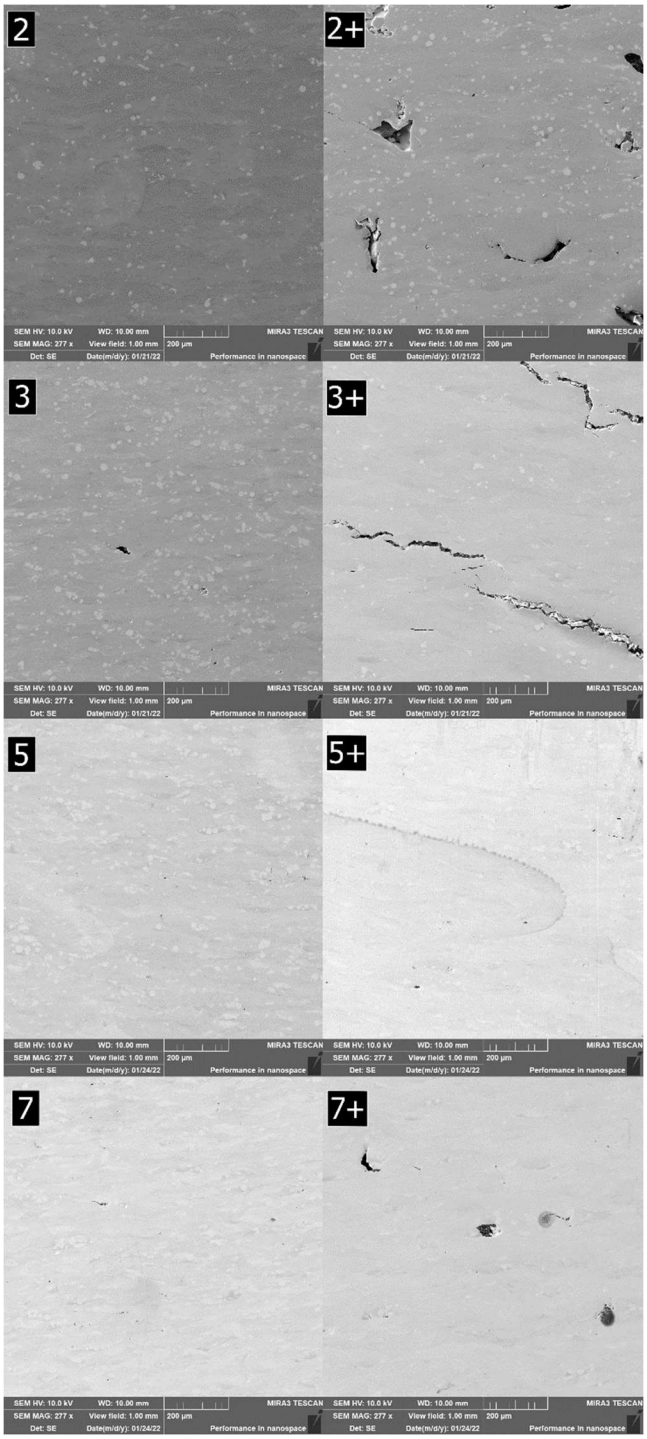

Figure 12: polished surfaces of un-heat-treated samples

The results from the un-heat-treated sample EDS maps are shown below in Figure 13. These results back up the previous observation that the samples are generally not well mixed, as there are different stark phases of element-heavy areas spread sporadically across the surfaces of them all. They are generally composed of four or more phases, and many of them have pockets of concentrated phases that imply an area of unmixed powder with nearly 100% one of the three base metals.

The estimated elemental percentages of each sample from the EDS map reports are compiled below in Table 2. Because the addition of hafnium carbide was so low that the software would likely report negligible amounts with high error, it is not estimated for the hafnium carbide samples. The percentages consistently show under-representation of rhenium. It is difficult to speculate why the rhenium content may be lower, although it could potentially have to do with the non-spherical powder not wiping as well, resulting in a slight imbalance in the alloy composition per wipe during printing. The percentages also consistently overestimate the amount of molybdenum in the base alloys and report a lower amount closer to or lower than was mixed for the hafnium carbide alloys. Again, it is difficult to pinpoint a cause, although it may be related to hafnium carbide's high melting point. If the samples got hotter, it is possible that some amount of molybdenum was vaporized during printing. Regardless, the results are consistent, despite an imperfect mixing technique and use of non-spherical rhenium powder.

Table 2: Un-heat-treated EDS elemental percentages

	Element wt%		
Alloy	W	Mo	Re
2	19.69	72.01	6.48
2+	22.43	68.93	5.65
3	28.23	58.73	13.05
3+	35.4	50.72	13.88
5	49.12	37.01	13.86
5+	54.79	30.6	14.61
7	64.62	29.04	6.34
7+	77.77	15.32	6.91

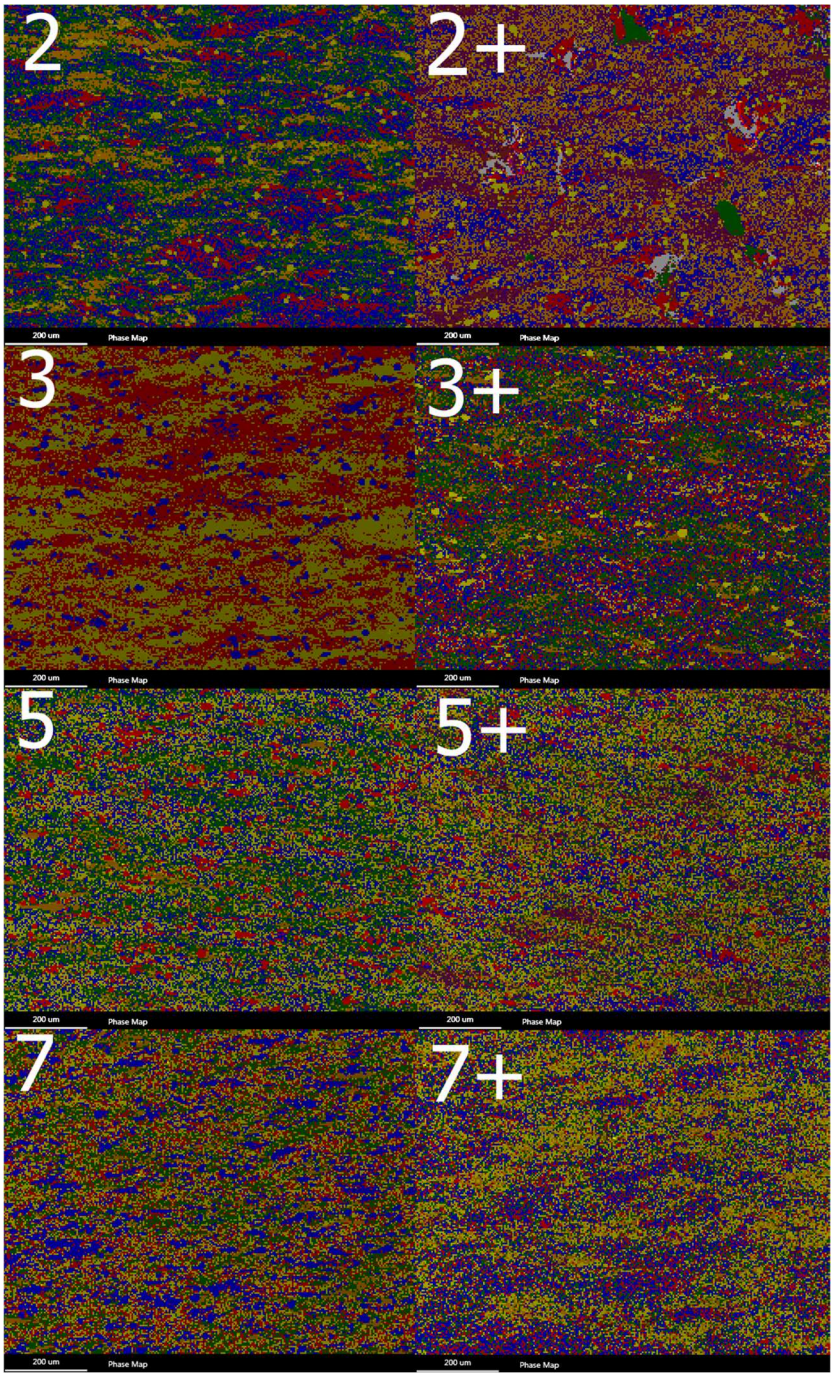

Figure 13: EDS maps of un-heat-treated samples

Porosity measurements were also taken for the un-heat-treated samples, to compare to the heat-treated samples later on. Optical microscopy images were taken of the representative polished surfaces of the samples, and the ZEISS ZEN core software estimated the pore number and size relative to the image. An example of this result is shown in Figure 14, which uses sample 3. The areas marked in red are the pores, and the porosity is calculated in percentage of colored in pixels. The software tolerance has been adjusted to not include surface scratches.

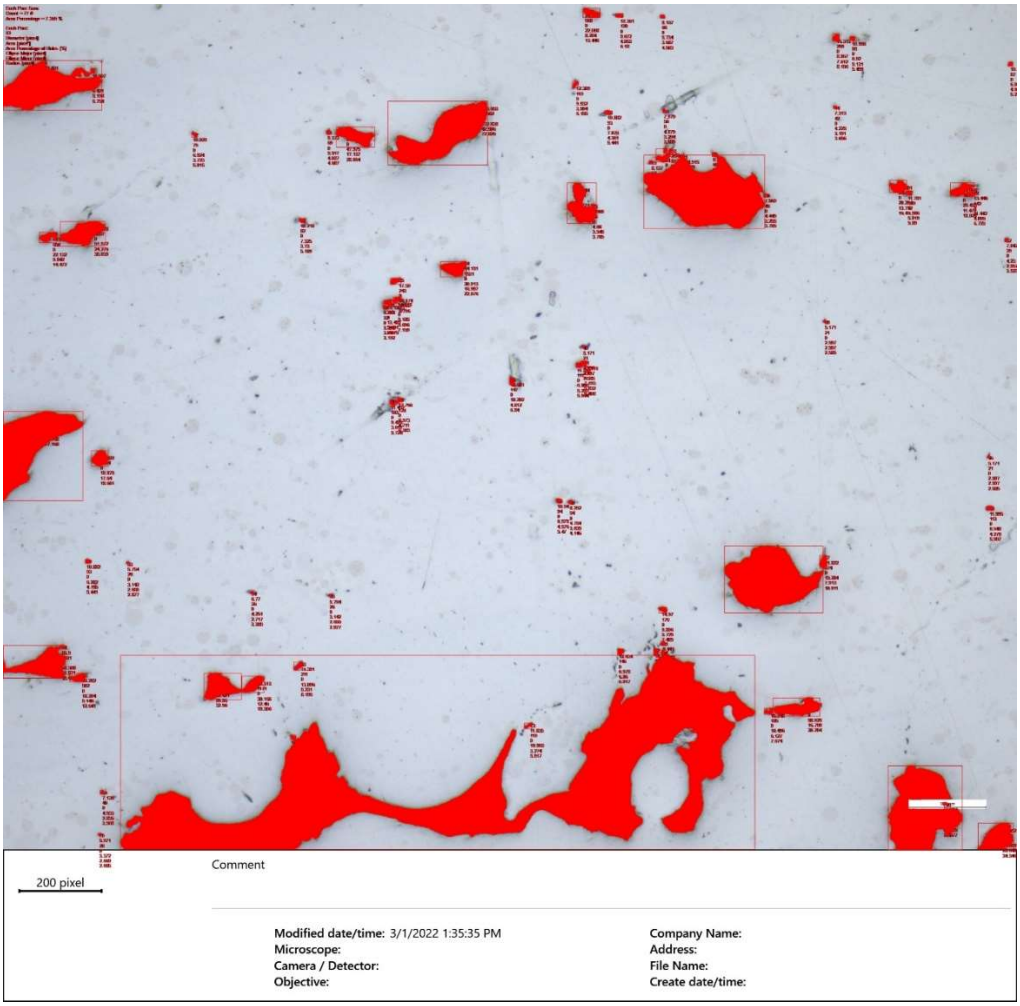

Figure 14: Porosity measurement example using sample 3

Results for all eight samples' average porosity are shown below in Table 3. The samples generally have low porosity even before heat treatment, with five of the eight averaging at under 1%. However, samples 2+, 3, and 3+ were well above this, with sample 3 having nearly 4% porosity.

Table 3: Pre-heat treatment porosity percentages

Alloy	Average Porosity %
2	0.629
2+	3.621
3	3.788
3+	1.41
5	0.244
5+	0.18
7	0.797
7+	0.445

3.3 Post-Heat Treatment Microstructure

When the samples returned from heat treatment, one of each was set aside for further microstructure analysis to compare to the un-heat-treated samples. The polished surfaces of the heat-treated samples are presented below in Figure 15. There is still relatively little notable porosity for almost all the samples, and the cracking which marred the hafnium carbide samples before has been severely reduced, as shown by the nearly healed crack in the 5+ sample. The 2+ sample also had sporadic porosity across the surface, despite the original sample having areas with little to none. It is possibly an outlier specimen, as it is worth noting that the strength data presented in sections 3.4 and 3.5 do not exhibit an unusual weakness for that alloy.

The other important takeaway from Figure 15 is that the samples appear to have much improved diffusion. There are no longer speckles of unmixed metals all throughout, which all of the samples displayed in Figure 12 had. The increased homogeneity would lead to higher strengths, which was the anticipated result and the motivation for getting heat treatment done before mechanical testing.

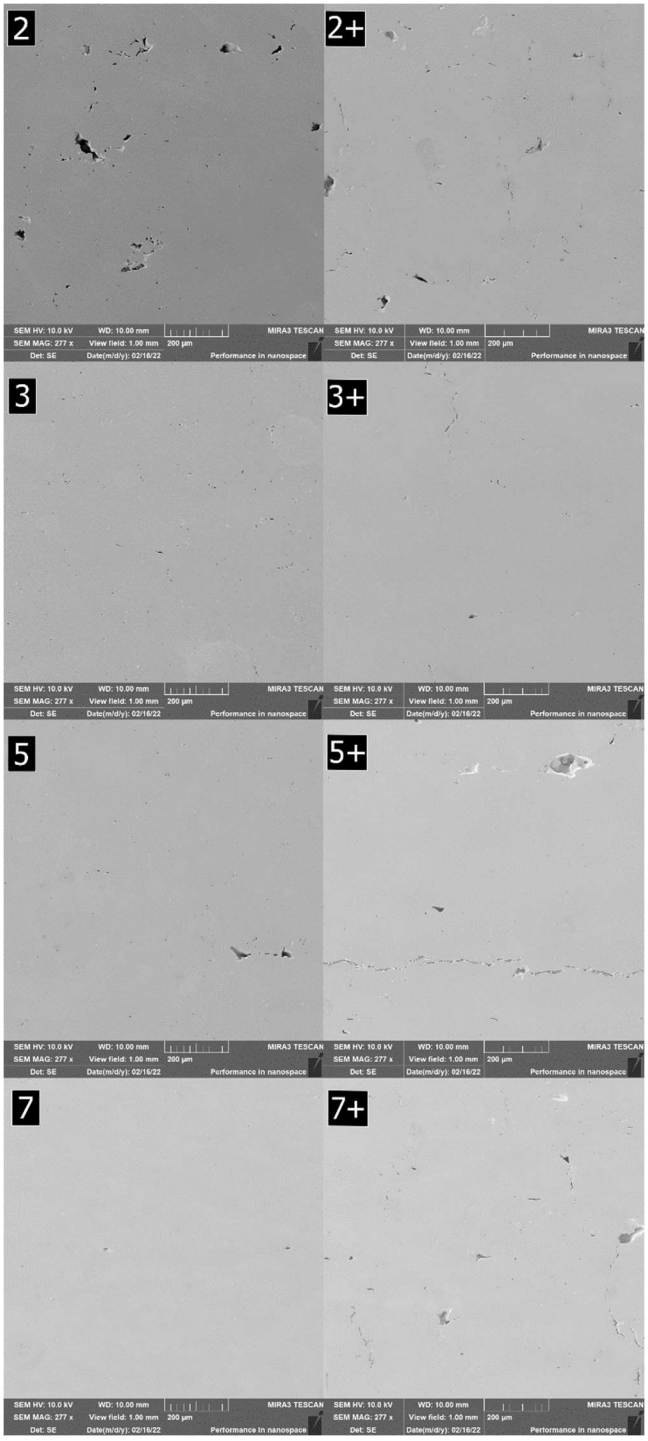

Figure 15: polished surfaces of heat-treated samples

EDS maps were taken for the heat-treated samples as well, and readily reflect the improved diffusion observed in Figure 15. The EDS maps below in Figure 16 display much more homogeneity, with phases more consistently mixed throughout. In fact, five of the eight samples displayed only one phase, and only one displayed three. Despite the 2+ sample exhibiting the least improved diffusion, there is still a notable improvement from before heat treatment in Figure 13, with four phases and pockets of concentrated phases.

The estimated alloy content of each sample's EDS map is listed below in Table 4. The results are similar to those from the un-heat-treated samples. Again, the rhenium content is noticeably under-represented in all cases, and in most cases the molybdenum content is lower in the hafnium carbide samples than in the base alloy samples. It makes sense that there would be little difference between the results pre- and post-heat treatment because the heat treatments were intended to improve mixing and heal defects, not affect the elemental compositions.

Table 4: Heat-treated EDS element percentages

	Element %		
Alloy	W	Mo	Re
2	24.3	69.07	6.63
2+	26.95	66.51	6.53
3	33.92	51.55	14.53
3+	37.25	48.41	14.34
5	57.16	28.05	14.79

5+	51.95	34.27	13.78
7	75.08	17.27	7.68
7+	76.35	15.47	8.18

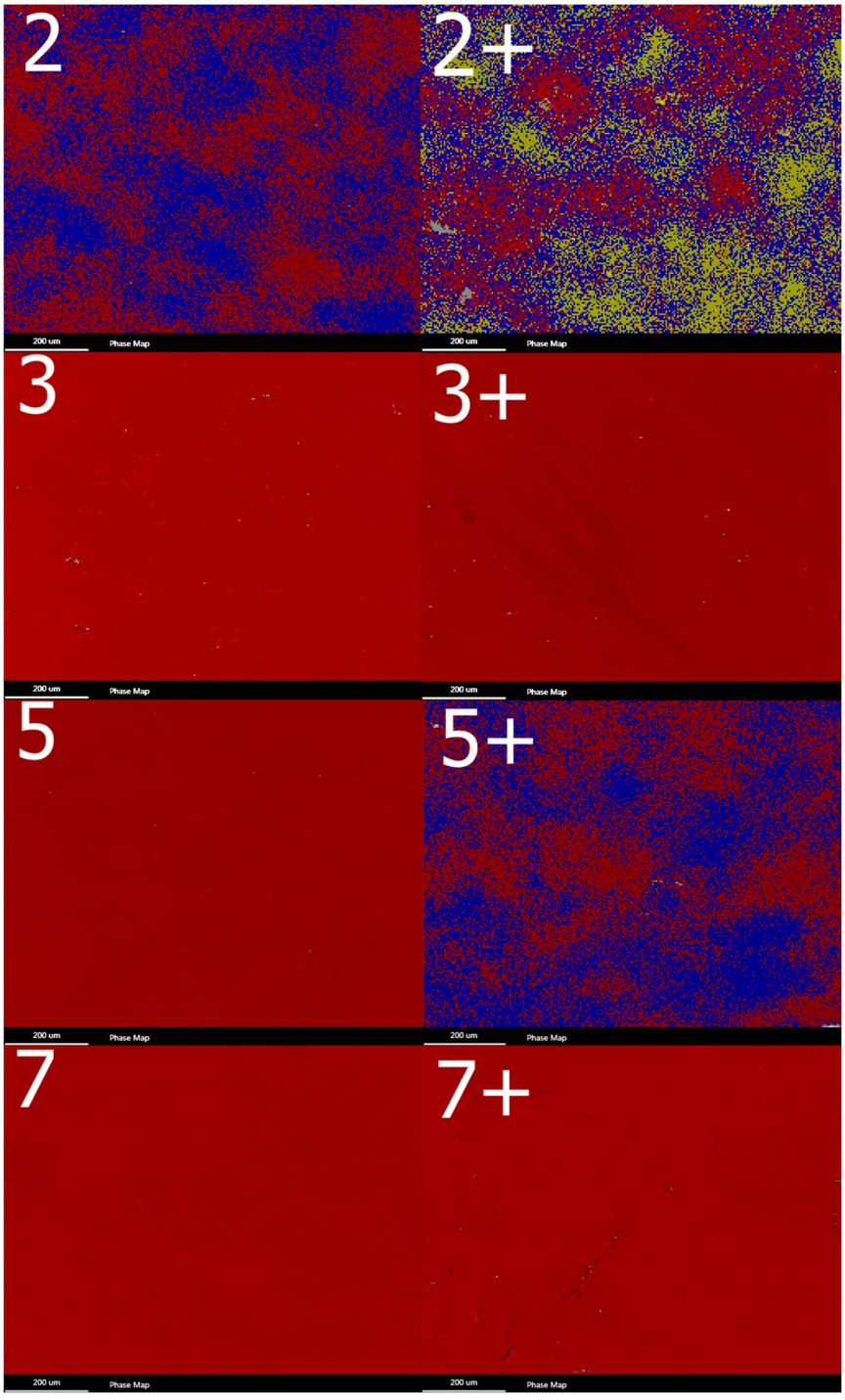

Figure 16: EDS maps of heat-treated samples

Porosity measurements were taken with the heat-treated samples as well. The results are presented below in Table 5. Generally, the trend is decreased porosity as compared to the un-heat-treated specimens, as expected. The exception to the improvement in this case is the 5+ sample, which now has notable porosity despite the original sample having little to none. While it is initially unclear if the un-heat-treated sample was unusually good or if the heat-treated sample is unusually poor, the strength data presented in sections 3.4 and 3.5 will shed light on the overall quality.

Table 5: Heat treated porosity percentages

Alloy	Average Porosity %
2	0.431
2+	2.881
3	0.975
3+	0.628
5	0.413
5+	1.113
7	0.542
7+	0.855

Grain size analysis was done with etched samples using SEM images with high contrast settings to better show the grains. An example of the line counting method is shown below in Figure 17 using a 5 sample. Because the grain sizes varied greatly, the three lines' results were averaged for a more accurate estimation. The average number of grains per line was found and then divided by the view field to calculate grain size.

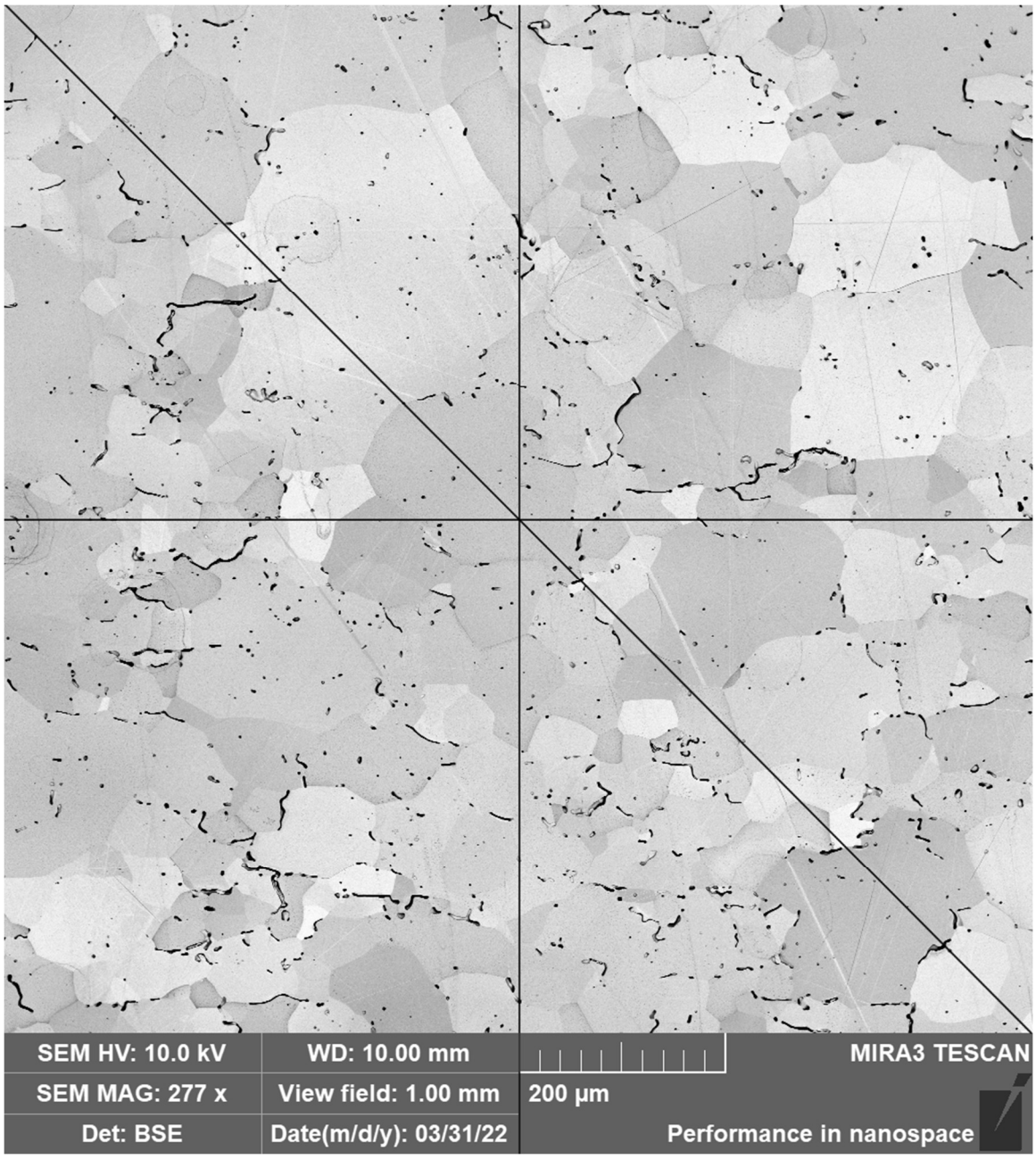

Figure 17: Grain size counting method

The results from the grain size estimation analysis are listed below in Table 6. Across the board, the grain sizes for the hafnium carbide samples were larger than their

base alloy mates, sometimes by nearly double. For the samples with 20 wt% and 70 wt% tungsten, the grain sizes are smaller than in the ones with the intermediate amounts of tungsten. This is most notable in the base alloys 2 and 7 but holds up to a less notable extent in the hafnium carbide 2+ and 7+ alloys as well. The link appears to be the rhenium content, because the 2 and 7 samples contain 10 wt% rhenium, while the 3 and 5 samples contain 20 wt% rhenium. Grain size tends to increase with increasing rhenium content.

Table 6: Average grain size per alloy

Sample	Average Grain Size (μm)
2	50.4
2+	116.8
3	93.9
3+	141.4
5	73.4
5+	127.2
7	53.2
7+	88.9

3.4 Three-Point Bend Data

Bend data was calculated with three replicates per alloy and the resulting stress and strain values were averaged. The results from the base and hafnium carbide alloy tests are listed below in Table 7 and Table 8 respectively.

The base alloys exhibit moderately low strain to failure, which decreases with increasing tungsten content. This is the expected result, as tungsten is a brittle material at room temperature, and molybdenum can be somewhat ductile at room temperature.

The average yield strengths start out lower than that of pure tungsten at room temperature (750 MPa) but are notably higher than rhenium and molybdenum (290 and 400 MPa respectively). With increasing tungsten content, there is initially an increase in yield strength, and then a decrease which leads to a steep drop-off with the 7 samples. If the samples are analyzed in terms of rhenium content instead, the results are clearer. Rhenium's aforementioned softening effect in molybdenum occurs up until around 20 wt%, at which point it hardens and strengthens the material instead. Thus, the two alloys with 20 wt% rhenium are stronger than those with only 10 wt%, which are still in the softening region.

Table 7: Base alloy three-point bend strength and strain data

Alloy	Failure Strain (-)	Average Failure Strain %	Strength (MPa)	Average Strength
2	0.180654		591.7055434	
2	0.164929		529.3761009	
2	0.181305	17.5629264	597.8872382	572.9896275
3	0.196698		692.1250128	
3	0.154212		759.3528785	
3	0.16403	17.1646638	582.1004071	677.8594328
5	0.130258		561.9196594	
5	0.141652		481.9538397	
5	0.14098	13.7630052	555.0454509	532.9729834
7	0.079502		292.3045964	
7	0.104355		329.1017874	
7	0.080727	8.8194595	296.5744367	305.9936068

For the hafnium carbide samples, the trends are less clear. The failure strains do not continually decrease with tungsten content, as the 7+ samples had higher failure strains than the 5+ samples. Likewise, because molybdenum content directly decreases with increasing tungsten, there is no trend there. There could potentially be a correlation between the rhenium content, as the two samples with higher rhenium (3+ and 5+) had the lower failure strains, but by a small margin.

The yield strengths for these samples are notably lower, maxing out at lower than molybdenum's yield strength. Rather than increasing with tungsten content, the strength instead decreases sharply, up until the 7+ samples where it increases again. This time, the

two strongest values are for the samples with the most molybdenum (2+ and 3+), rather than the higher rhenium.

Table 8: HfC alloy three-point bend strength and strain data

Alloy	Failure Strain (-)	Average Failure Strain %	Strength (MPa)	Average Strength
2+	0.113398		332.4313703	
2+	0.108085		436.114452	
2+	0.121066	11.4182834	345.662263	371.4026951
3+	0.127578		342.2906036	
3+	0.117566		364.0612712	
3+	0.089528	11.1557127	326.8804173	344.410764
5+	0.089415		216.9502262	
5+	0.062398		216.3657696	
5+	0.074301	7.5371175	205.736009	213.0173349
7+	0.092794		278.8390099	
7+	0.127981		385.5079981	
7+	0.124425	11.5066846	215.5383386	293.2951155

The average strength values are plotted for both the base and hafnium carbide alloys below in Figure 18. As discussed from the data tables, the two alloy sets exhibit opposite trends. Although this was initially unexpected because hafnium carbide was reported to strengthen grain boundaries and encourage transgranular fracture in molybdenum, it may be explained by the presence of rhenium in the alloy. While hafnium carbide is known to assist with high temperature tension strength in molybdenum-rhenium alloys, it was noted to cause some embrittlement at lower temperatures [42], and these tests were carried out at room temperature.

There is some discussion to be had on potential outliers, and how they might have affected the data. For example, of the 3 samples, the individual strength values from the bend tests were 692, 759, and 582 MPa. Also, of the 7+ samples, the individual strengths were 279, 386, and 216 MPa. With such a large variation between the three values in some of the sets, it is possible that one of them may, due to some cause such as a defect, may be abnormally stronger or weaker, and not representative of the material. While it is impossible to say for sure which, if any, would be the outliers, it can be helpful to keep in mind when observing the trends. If the strongest of the 7+ samples was removed, which was over 100 MPa stronger than the other two in its set, the below curve would look very different.

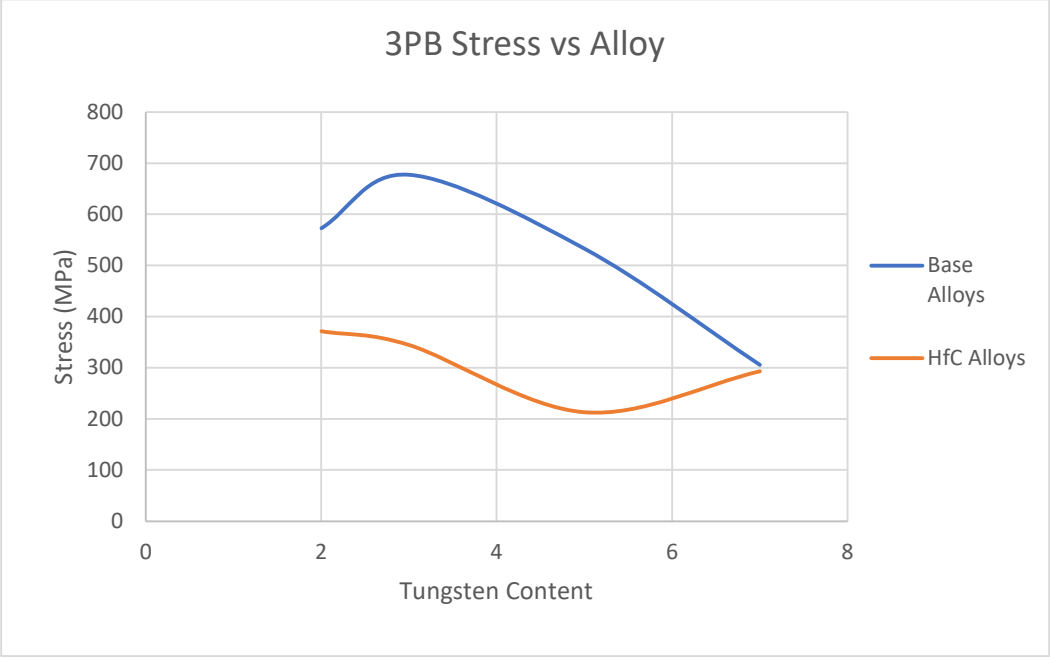

Figure 18: Average three-point bend stresses

Broken pieces of the bend specimens were imaged with an SEM to observe fracture mode and microstructure. Fracture surfaces are presented in Figure 19 below. The grains are visually larger in the hafnium carbide specimens than in the base alloy specimens. Also, the grains are notably more refined in the 2 and 7 samples.

The more polygonal shapes that dominate specimens like samples 5 and 7 are intergranular fracture. These specimens broke along the grain boundaries, which is indicative of brittle fracture. However, the flatter, more textured regions especially obvious in parts of sample 2 and 3+ show transgranular fracture. These breaks went straight through grains, which is indicative of more ductile fracture, and typically of stronger grain boundaries. There are slightly more areas of transgranular fracture visible in the base alloy samples than in the hafnium carbide samples, which explains why the base alloy samples had slightly higher strains than the hafnium carbide ones did.

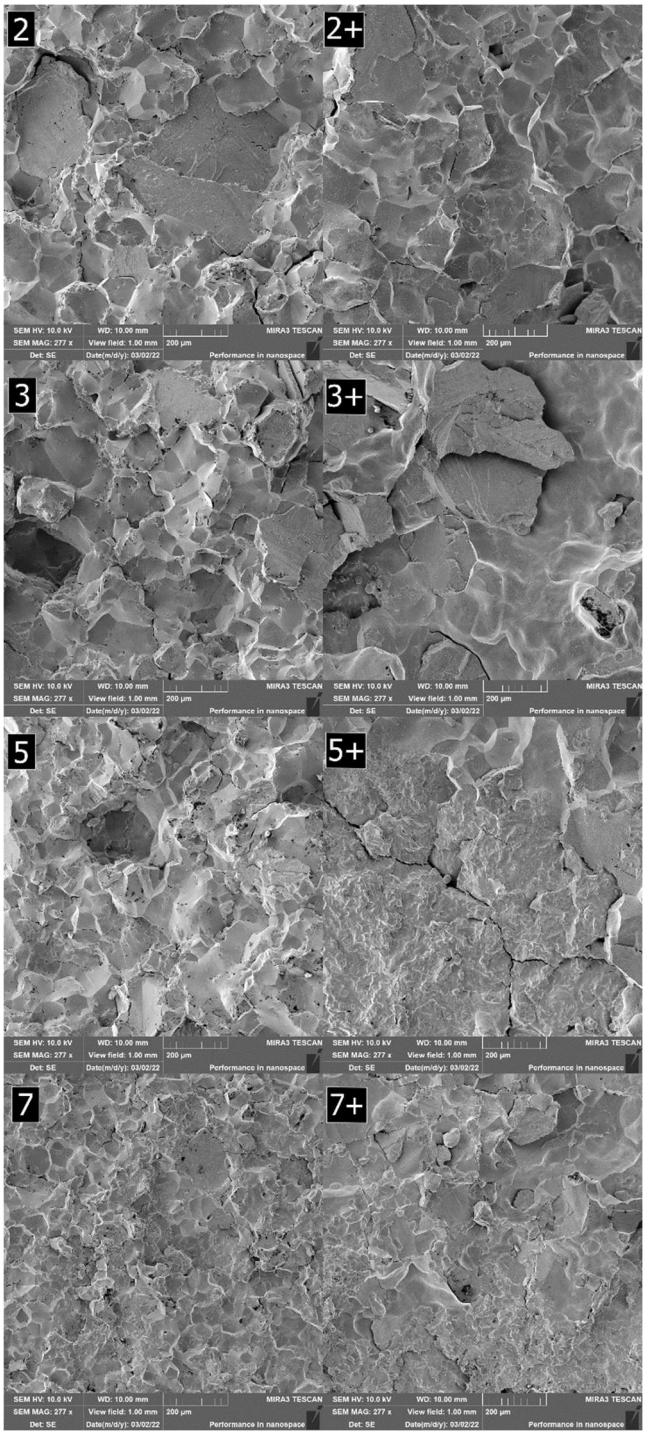

Figure 19: Bend test fracture surfaces

A representative fracture surface from each alloy was imaged in sections to estimate the percentage of transgranular fracture. Because the samples had cross sections of 2x4 mm, they were sectioned into eight 1 mm view field images. An example of the measurements is shown below using a 3 sample in Figure 20. The combined percentages are reported in Table 9 below. In the base alloys, the trend is clear. As the tungsten content increases, the percentage of transgranular grains decreases. In these alloys, it appears to be linked to higher molybdenum content. However, in the hafnium carbide samples, the trend is less obvious. There is not a clear pattern, although it is worth noting that, while most base and hafnium carbide sample partners had similar percentages, the 7+ is markedly higher than the 7.

As compared to the bending strengths listed in Table 7 and Table 8, the percentage of transgranular grains in the base alloys appear to roughly follow the reported strengths. The molybdenum-heavy samples are both the stronger samples and the samples with the higher proportion of transgranular grains. Meanwhile, the hafnium carbide samples follow a similar trend shape, but the strongest sample (the 2+) has the second lowest percentage of transgranular grains. The association of strengths and transgranular grains is less apparent in these alloys than in the base alloys.

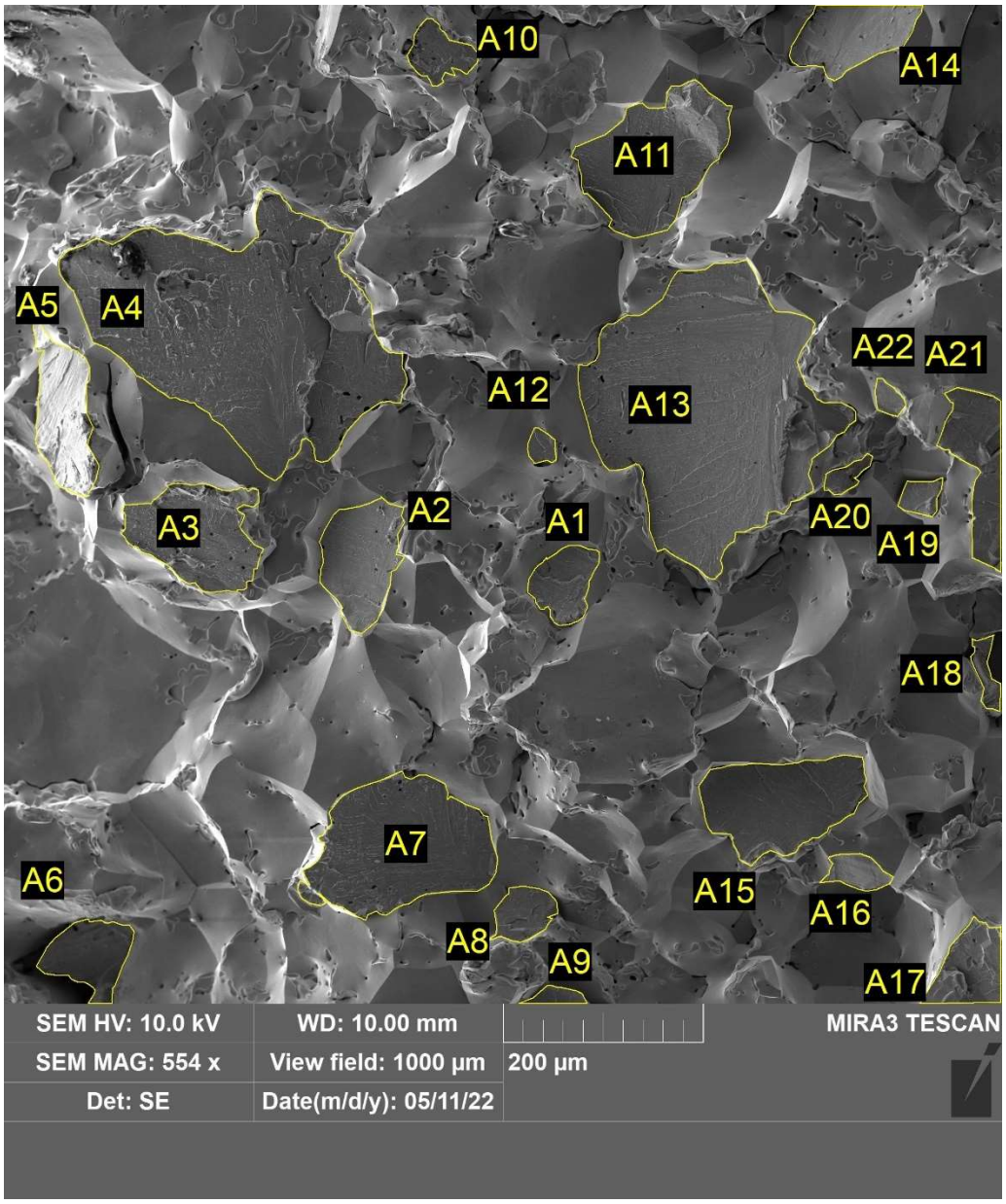

Figure 20: Transgranular area measurement

Table 9: Percent transgranular grains

Sample	Percent Transgranular
2	15.97
2+	10.71
3	14.51
3+	11.29
5	5.84
5+	9.49
7	2.87
7+	13.57

It is also possible to see the distribution of hafnium carbide nanoparticles at the grain boundaries on the fracture surfaces. A compilation of the nanoparticles in the hafnium carbide samples is shown below in Figure 21. The distribution is consistently spread out, and not concentrated in one place, which is ideal.

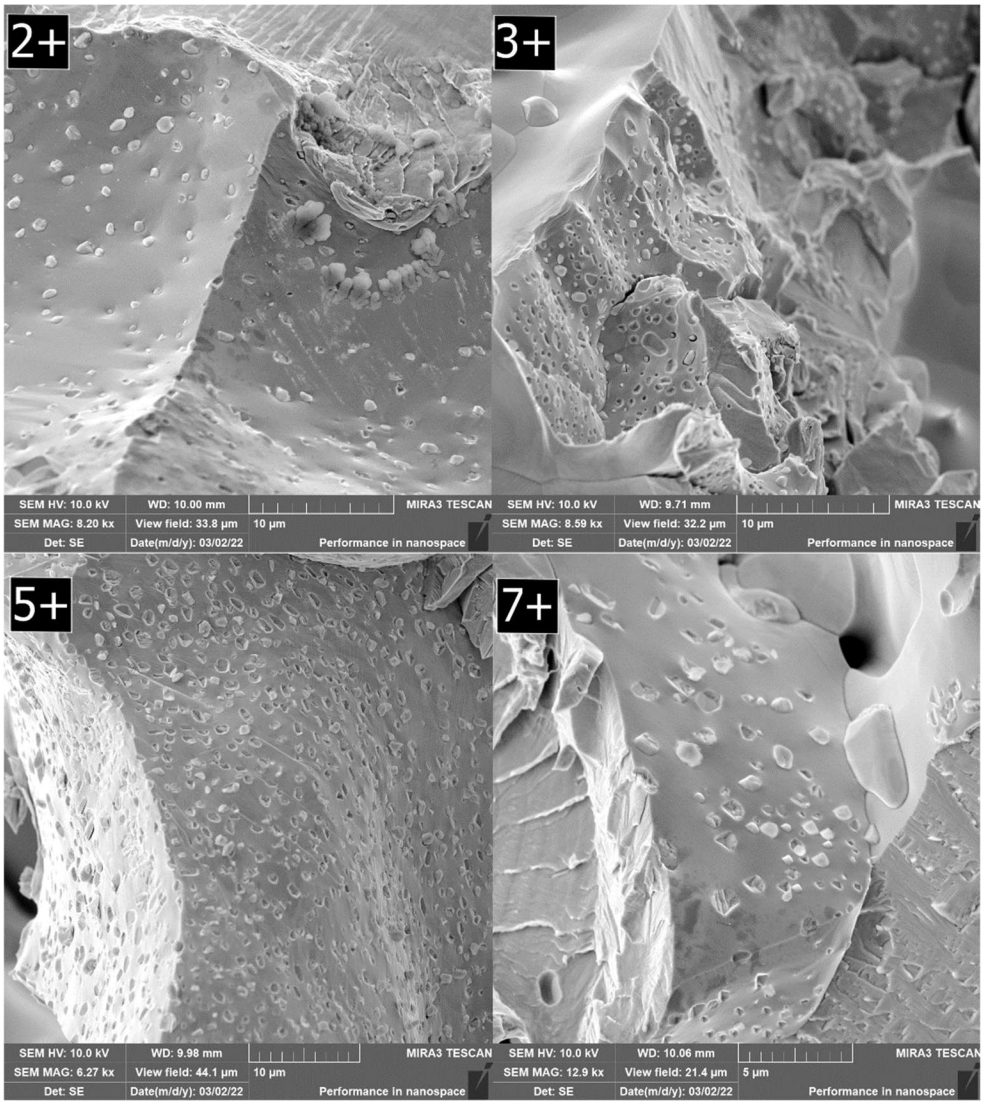

Figure 21: HfC distributions on fracture surfaces

3.5 Compression Data

Cylindrical specimens for each alloy were also crushed to obtain the Young's modulus and compression yield stress. Results from these tests for the base and hafnium carbide alloys are listed in Table 10 and Table 11, respectively.

The base alloy Young's modulus increases steadily with increasing tungsten content, before dipping slightly for the 7 sample. Based on the alloy content per sample, this does not appear to be directly linked with the amount of tungsten, molybdenum, or rhenium. The sample with the highest Young's modulus for this set was the 5, at 345.92 GPa. Comparing the moduli to the failure strains noted in the bend test data, they appear to have an opposite relationship. As the tungsten content increased in the bend specimens, the failure strains decreased. However, as the tungsten content increased in the compression specimens, the Young's moduli generally increased.

The 0.2% yield strength follows a similar trend to the three-point bend test data. The strengths are similar, if a little bit lower, and they increase before dropping off again with the 7 sample. The strongest sample for this set was the 5, at 583.88 MPa. In comparison, the strongest sample for the bend data was 3, at 677.86 MPa – a roughly 94 MPa difference.

Table 10: Base alloy compression data

Alloy	Young's Modulus (GPa)	0.2% Yield Stress (MPa)
2	109.199	418.27

3	246.52	478.25
5	345.91	583.88
7	318.61	390.94

The hafnium carbide alloys follow a more similar pattern to the base alloys than to the bend data's hafnium carbide alloys. Once again, the strengths are lower than that of the base alloys, up until 7 and 7+ alloys, where the hafnium carbide sample was stronger by roughly 107 MPa.

The Young's modulus follows no clear pattern regardless of which base metal content it is measured by. However, it is worth noting that the 7+ sample has a notably higher modulus of elasticity than the others, more than double the second highest value. In comparison to the base alloy Young's modulus results, while the 2+ is higher than the 2, the rest of the values are much lower than the base values. This follows with the bend test results that showed the hafnium carbide samples exhibiting lower failure strains. However, these alloys do not show the roughly opposite behavior that the base alloys did between the Young's moduli and failure strains. Where the failure strains were generally the same except for the lower 5+ sample, the compression test elastic moduli vary greatly, and the 2+ has the lowest modulus.

Table 11: HfC alloy compression data

Alloy	Young's Modulus (GPa)	0.2% Yield Stress (MPa)

2+	120.68	212.82
3+	171.73	412.7
5+	148.38	471.2
7+	296.65	497.93

As a comparison for the compression data, specimens of W-25Re and W-25Re-1ZrO_2 were also broken. The samples were prepared in the exact same manner as the W-Mo-Re samples were, for consistency. The results of these tests are shown in Table 12. W-25Re is a very strong material, and thus a good benchmark comparison for the strength of the ternary alloys. The addition of the nanoparticle in this case did as expected and increased the yield strength of its alloy. However, the Young's modulus was notably lower with the nanoparticle additive than without. The only ternary that was close to the same yield strength was 5, at 583.88 MPa versus W-25Re's 671.23 MPa and W-25Re-1ZrO_2's 696.89 MPa.

Table 12: W-Re and W-Re-ZrO2 comparison

Alloy	Young's Modulus (GPa)	0.2% Yield Stress (MPa)
W-25Re	314.22	671.23
W-25Re-1ZrO2	218.54	696.89

Average yield stresses were plotted versus tungsten content for the compression data as well. The trends here in Figure 22 are very different from those observed in the three-point bend testing. The base alloy curve is similar, although with 5 being the strongest sample as opposed to 3. However, the hafnium carbide curve has opposing behavior. While the bend test results showed a concave sort of relationship where the strength decreased and then increased again, the compression data shows that the strength started out low, jumped to nearly double the strength with the next alloy, and then continued to steadily increase at a much more reserved rate. Although there are fewer samples to compare for the compression tests, it is once again possible that outlier specimens could be affecting the data, which could help explain some of the less clear trends, especially the notably strong 7+ sample.

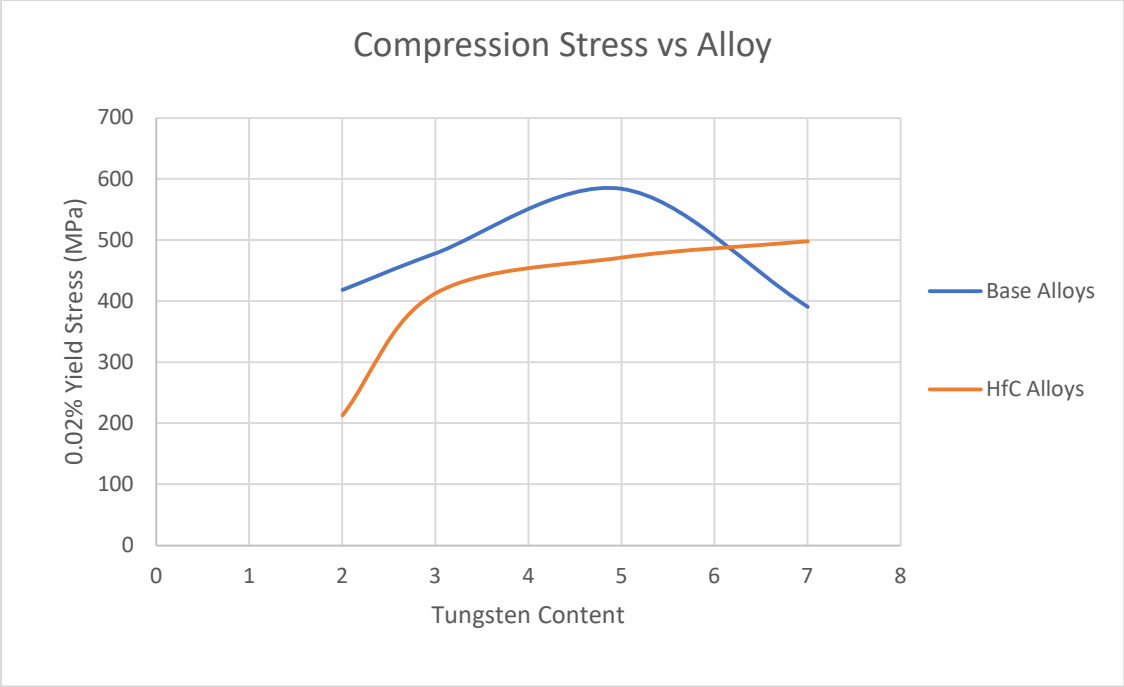

Figure 22: Average compression stresses

The crushed samples were also loaded into pucks and polished for SEM analysis, to observe any potential differences between the microstructure before and after crushing. The maps are presented below in Figure 23. As expected, they look similar to the un-crushed maps from Figure 16. However, the previously visible grains are now notably flattened. Additionally, the un-crushed samples displayed only three of eight alloys with multiple phases, and only one of the three had three phases, while the other two only had two phases. The crushed samples in Figure 23 show that four of the eight samples read as multi-phase, with two of them having three or more phases.

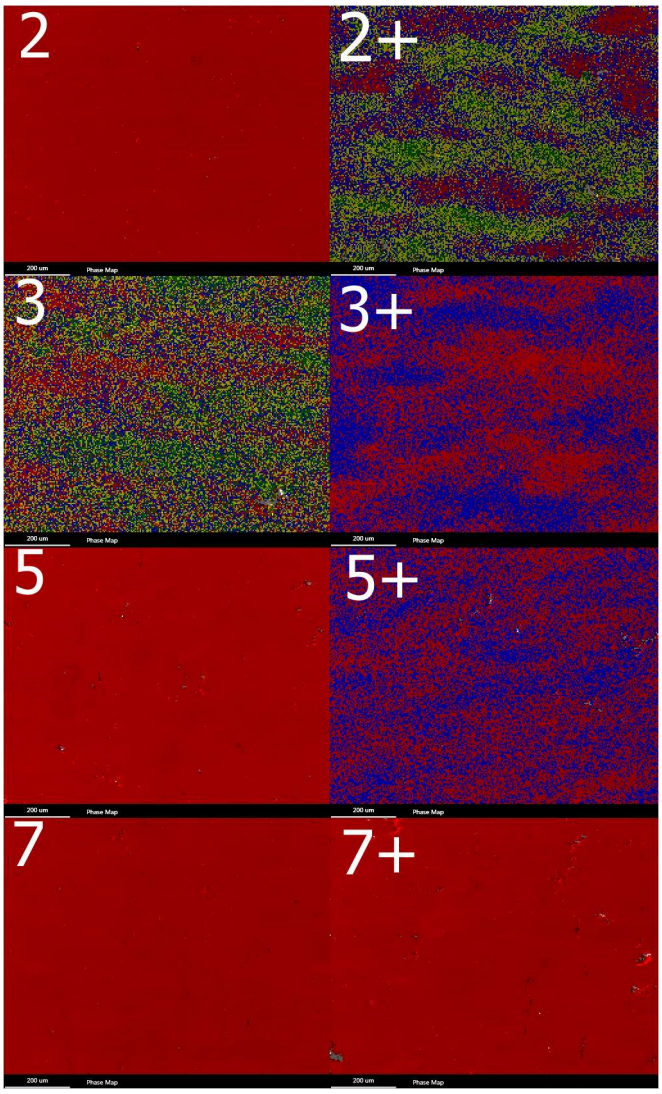

Figure 23: Crushed sample EDS maps

3.6 EBSD

EBSD maps were taken of each of the polished, etched base alloy samples. The EBSD maps reported on the grain size across the samples, showed the distribution of grain orientations, and noted the material structure, which confirmed that the samples were BCC as predicted.

Three maps were taken of each specimen in order to lessen error. One map of each of the base alloys is shown below in Figure 24. In binary tungsten-molybdenum alloys, grain size tends to refine with increasing tungsten content [61]. Additionally, alloying other metals with molybdenum tends to decrease its grain sizes [15]. However, the addition of rhenium appears to have enlarged grains with increased concentration. As observed in the previous grain calculations, the samples with 20 wt% rhenium exhibit visibly larger grain sizes than those with only 10 wt% rhenium. Additionally, the lack of large concentrations of similarly colored grains shows that there were no strong orientation preferences amongst the grains in any of the samples.

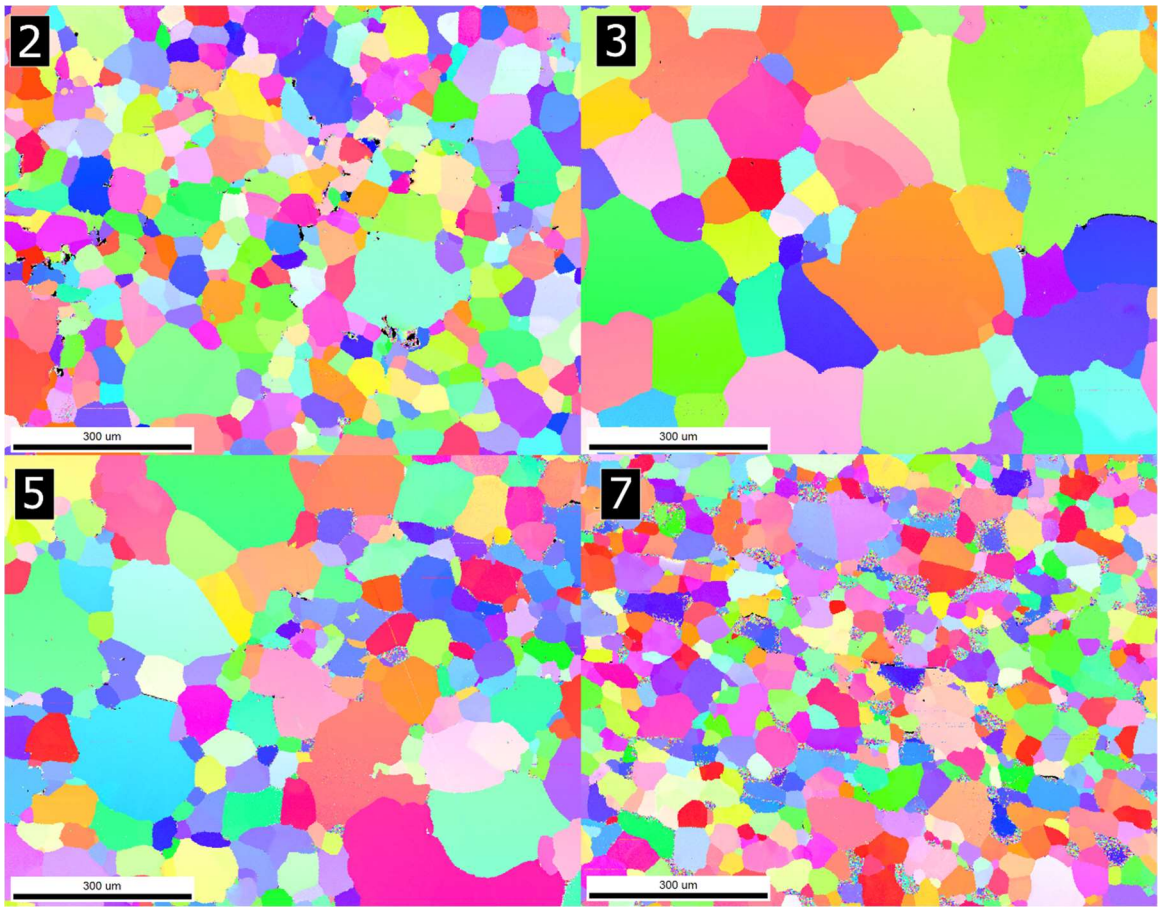

Figure 24: EBSD maps for base alloys

The average grain sizes are presented in Table 13. The estimations made by hand using the line method are compiled in Table 6 and follow the same trend but are generally smaller than the software measurements from EBSD. For example, the largest grains for both groups are those of the 3 samples, but the line calculations read 93.9 µm while the EBSD results read 159.84 µm. The difference could simply be a matter of which areas of the pucks were used to measure, or perhaps using more lines with the by-hand method would have reported numbers that more closely reflect the EBSD full-picture averages.

Table 13: Average grain size from EBSD

Sample	Average Grain Size (µm)
2	75.07
3	159.84
5	140.95
7	51.97

The EBSD software also had the option to reanalyze the EBSD maps to show maps of the kernel grain misorientations (KAM). The KAM maps are presented in Figure 25 below. The maximum selected misorientation angle was 5°, which would be shown in red. The overall misorientation was quite low, at mostly 0-2°, shown by the blue and green cool-colored maps. There are several instances of 3° misorientations, but few to no instances of 4-5°.

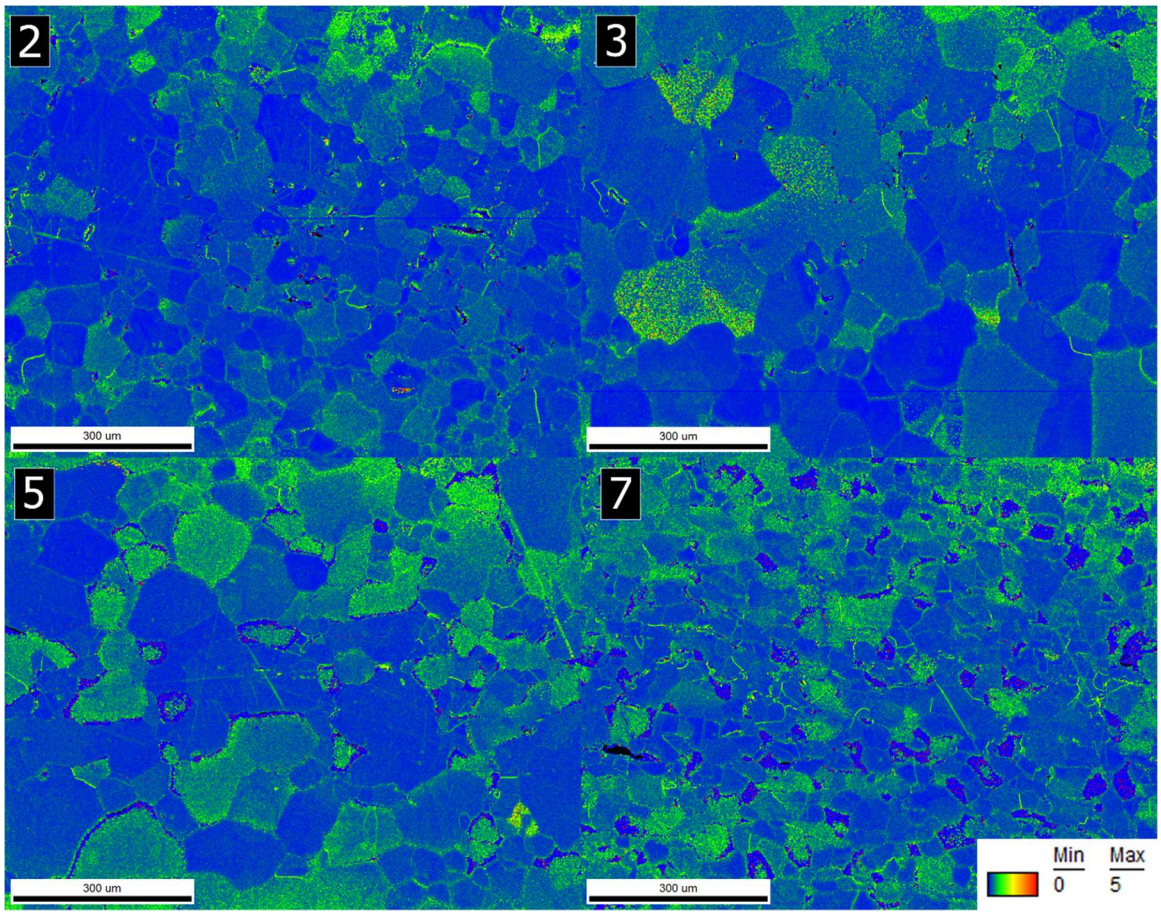

Figure 25: Base alloy grain misorientations

3.7 Implications of Results

There are several points to keep in mind when considering the results of the data presented in this thesis. By the nature of three-point bend tests, samples will fail near the center of their spans, on the outer surface that is experiencing tension. Due to this, the presence of any surface defects can affect the results. Also, because only three samples were tested per alloy, there is still some uncertainty in the averaged strengths. As discussed, there was variation between the sample sets from the bend tests, with some

samples having a difference of over 100 MPa from the others. Because there was not a larger number of samples tested, one cannot accurately determine which samples, if any, are the outliers, and thus cannot simply reject specific data points. More tests would need to be run to make more definitive statements.

Additionally, although the compression tests have fewer uncertainties than three-point bend tests and are thus more reliable, it is still worth noting that only one specimen was tested per alloy. Thus, while the compression tests are reliable in and of themselves, if any sample was poorer quality due to some printing defect, the results could be impacted. Future testing can and should be carried out to confirm and further expand on the information reported here.

IV. SUMMARY AND CONCLUSIONS

4.1 Summary

The tungsten molybdenum rhenium ternary space was explored using four alloys with varying amounts of each element, and four alloys with an additional 1 wt% HfC. Samples were printed using the LPBF technique. Microstructure on both un-heat-treated and heat-treated samples was characterized by polishing samples for microscopy. Heat treated samples were subjected to both three-point bend and compression tests to gauge their performance.

This work showed that metal additive manufacturing is a viable method for printing refractory metal alloys. The printed alloys had some defects such as cracks and

poor diffusion, which were largely eliminated through heat treatment. The heat-treated samples had favorable strengths, with up to 677.86 MPa in bending and up to 583.88 MPa in compression. The addition of hafnium carbide had an overall negative impact, with higher porosity, more cracking, and lower strengths. Different amounts or a different nanoparticle altogether may yield better results in further studies to come.

4.2 Conclusions

Tungsten molybdenum rhenium ternary alloys printed using laser powder bed fusion were shown to have fairly low porosity, some visible cracking, and consistent heterogeneity with spots of concentrated elements that speaks to poor mixing. The samples that underwent heat treatment generally resulted in lower porosity, healed cracking, and improved diffusion throughout. All of these help improve the strength of the samples.

Three-point bend tests of the samples showed a general increase and then decrease in strength with the base alloys, but a decrease and then increase in strength for the hafnium carbide samples. The strongest sample was sample 3 with a 677.86 MPa yield strength. Meanwhile the weakest sample was sample 5+ with only 213.02 MPa yield strength. The failure strain of the samples generally decreased with increasing tungsten content, as the materials grew more brittle. The largest failure strain was from sample 2 at 17.65% strain. The smallest failure strain was from sample 5+ at 7.54% strain.

The compression tests, on the other hand, showed similar trends with the base alloy, but exhibited different behaviors with the hafnium carbide alloys. In this case, the strongest sample was sample 5 at a 0.2% offset yield of 583.88 MPa, and the weakest was sample 2+ at 212.82 MPa. The base alloys' highest Young's modulus was for the 5 sample, at 345.92 GPa. The hafnium carbide alloys' values were notably lower, with the highest being the 7+ sample, at 296.65 GPa.

Increased rhenium content led to larger grains and higher strength overall. The compressive strength shows this most starkly, but the bending strengths are also higher for the median alloys. It may also be due to the 2 and 7 alloys being skewed predominantly towards molybdenum and tungsten respectively, both of which are brittle materials, instead of a more even mix of the three.

The addition of the hafnium carbide nanoparticle shifted the trends but was near-universally weaker. In three-point bending, its strongest sample (2+) was stronger than only the weakest of the base alloy samples (7), by a difference of roughly 65 MPa. It also appeared to embrittle the materials slightly, as the hafnium carbide samples generally showed somewhat lower strains and Young's moduli.

The grain sizes of the base samples were visibly more refined than those with hafnium carbide inclusions. Hand calculations estimated that the hafnium carbide samples were nearly double the size. Within both sets of samples, the grain sizes were the largest for the samples that had 20 wt% rhenium and were more refined in the samples

with only 10 wt% rhenium. The base alloy samples were analyzed by EBSD for more accurate grain size results. The scans confirmed that the 3 and 5 samples had the largest grain sizes, while the 2 and 7 had the most refined grains. The EBSD scans also confirmed that the material had BBC structure, and that grains had very low misorientation angles, of 0-3 degrees in general.

4.3 Contributions

This work provides several contributions to the sea of literary knowledge. These are:

1. Characterizes microstructure of a ternary space previously unstudied in metal additive manufacturing.
2. Reports the strengths of brand-new materials not found in the literature.
3. Discusses the use of nanoparticles in unique additively manufactured refractory metal alloys.

First, this work gives unique insights into the use of metal additive manufacturing for refractory metal alloys, the viability of the tungsten molybdenum rhenium ternary space, and the effects of additions of nanoparticles like hafnium carbide. It reports on the creation and resultant microstructure with characteristics distinctive to additive manufacturing processes. It has been shown that heat treated W-Mo-Re and W-Mo-Re-HfC samples created through LPBF can have little to no porosity, healed cracks, and homogeneous diffusion.

Second, the mechanical testing results were given. The characterization and strength data for these alloys was previously unreported and has now been studied in a multitude of ways. These alloys can have bending strengths of up to 677.86 MPa and compression strengths of up to 583.88 MPa.

Third, it was shown that the addition of 1 wt% hafnium carbide weakened and embrittled the alloys, with a maximum bending strength of 371.40 MPa and a maximum compression strength of 497.93 MPa. Thus, the hafnium carbide addition was either insufficient or too great. With this information now reported in the literature, the groundwork has also been set for continued study moving forward.

4.4 Future Research

In order to gain a true, complete understanding of this alloy space, different compositions of the tungsten, molybdenum, and rhenium should be printed. Because refractory metal alloys are typically desired for use in high-temperature applications, the alloys should be tested at elevated temperatures. The high-temperature strengths most likely exhibit different behaviors than room temperature. Classifying a wider variety of alloys at a range of temperatures will be vital for establishing a true understanding of the ternary space. Also, varying the energy input may yield a stronger parameter combination for developing the alloy using LPBF.

Heat treatments are significant for additive manufacturing methods, especially ones like laser powder bed fusion, where nearly every print will have some amount of

internal stresses, microcracks, or porosity. In order to ensure the ideal strength and performance of these alloys is found, different heat treatments should be investigated. Heating for longer amounts of time or at different temperatures could provide different results. Other heat treatment methods such as HIP may also yield important results.

Additionally, more research must be done to understand the effects of nanoparticles on refractory metal alloys. Experiments should be conducted with both more and less hafnium carbide, as well as other nanoparticles such as zirconium oxide or boron nitride, to help illuminate the unexplored space.

APPENDIX

When averages of several image measurements were used for calculations but only one was shown in the body of the paper for conciseness, the rest of the images are listed in the appendix, except for the sixty-three remaining transgranular grain images, available upon request.

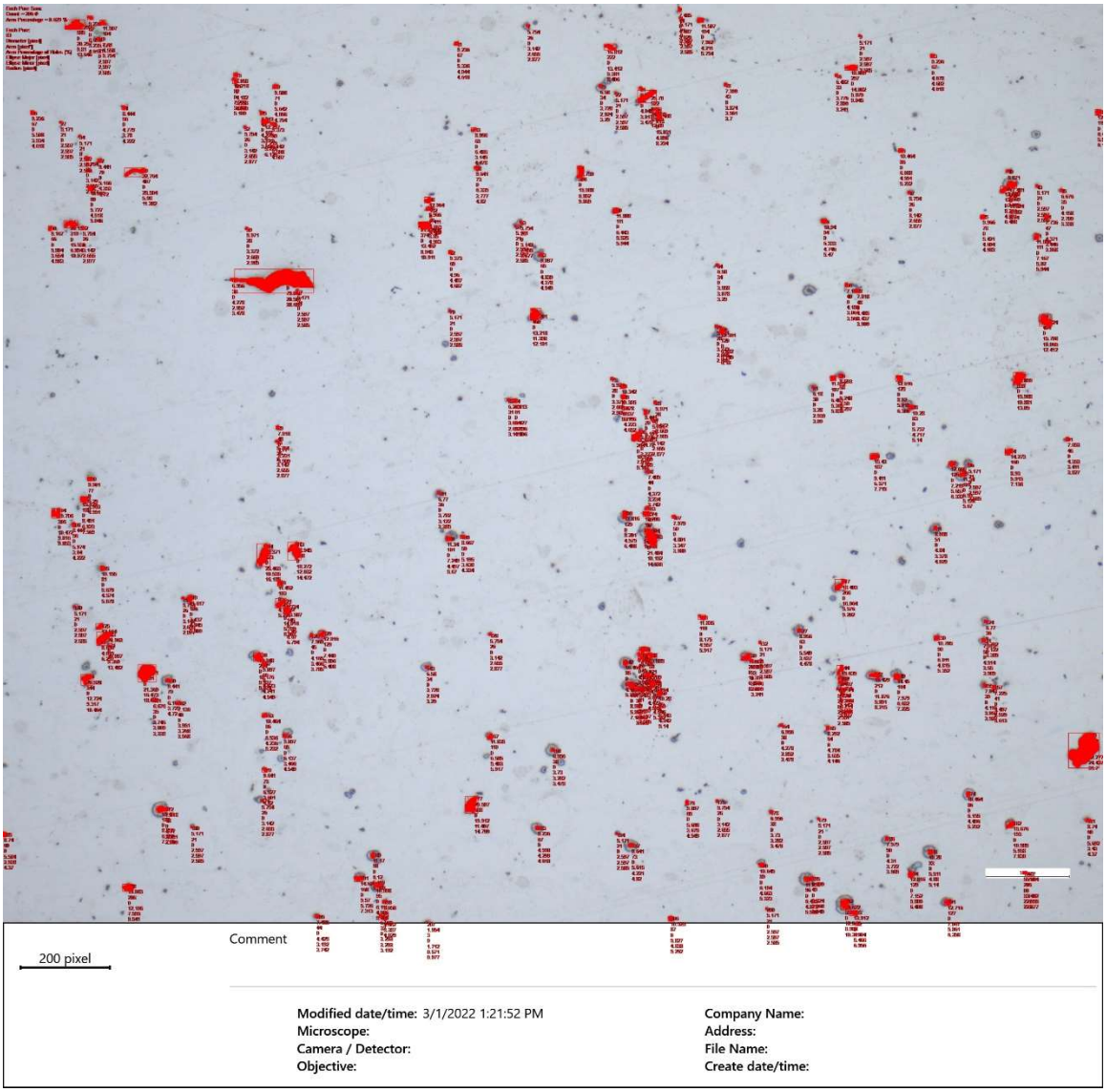

Figure A 1: Sample 2 porosity

Figure A 2: Sample 2+ porosity

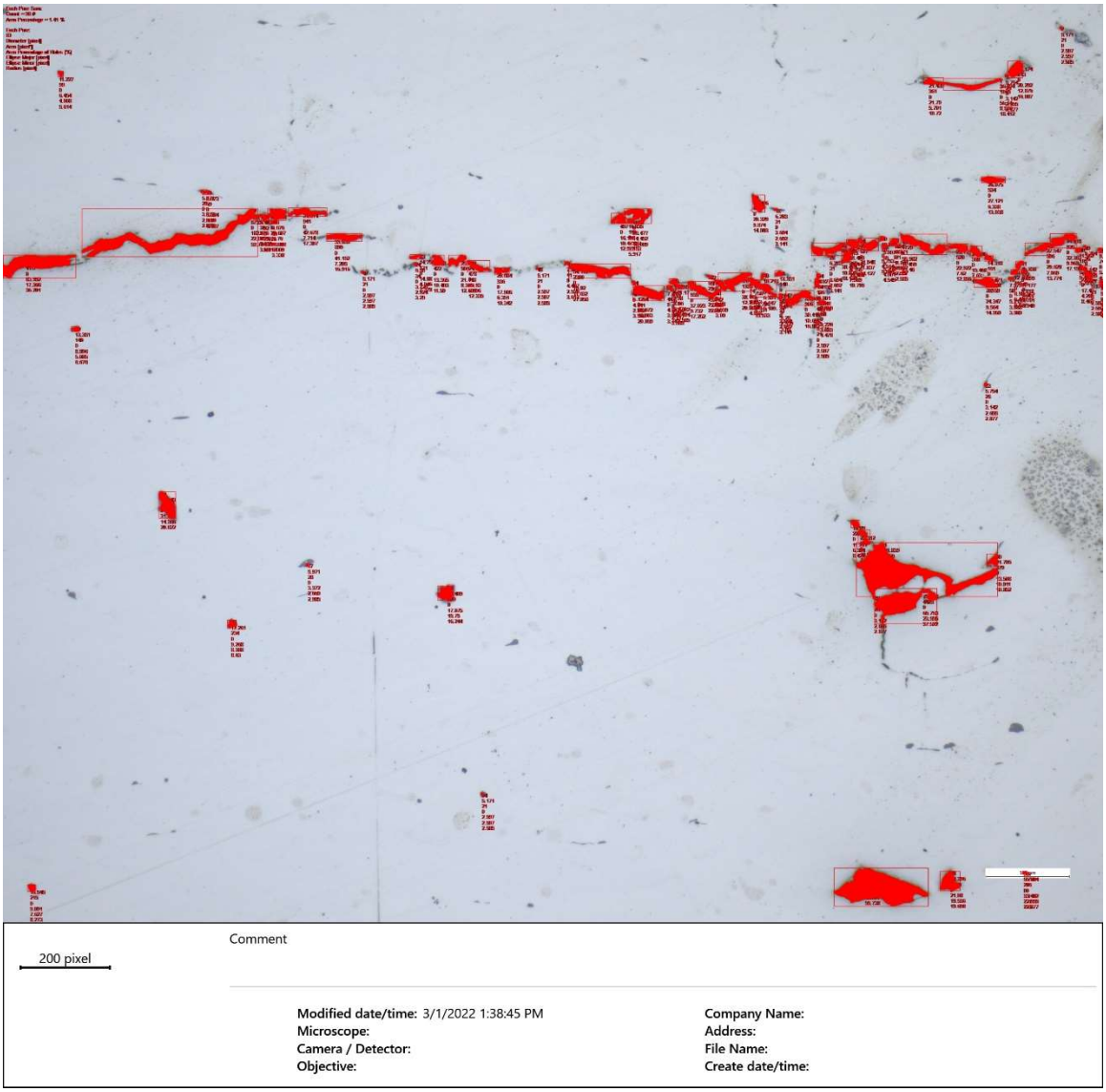

Figure A 3: Sample 3+ porosity

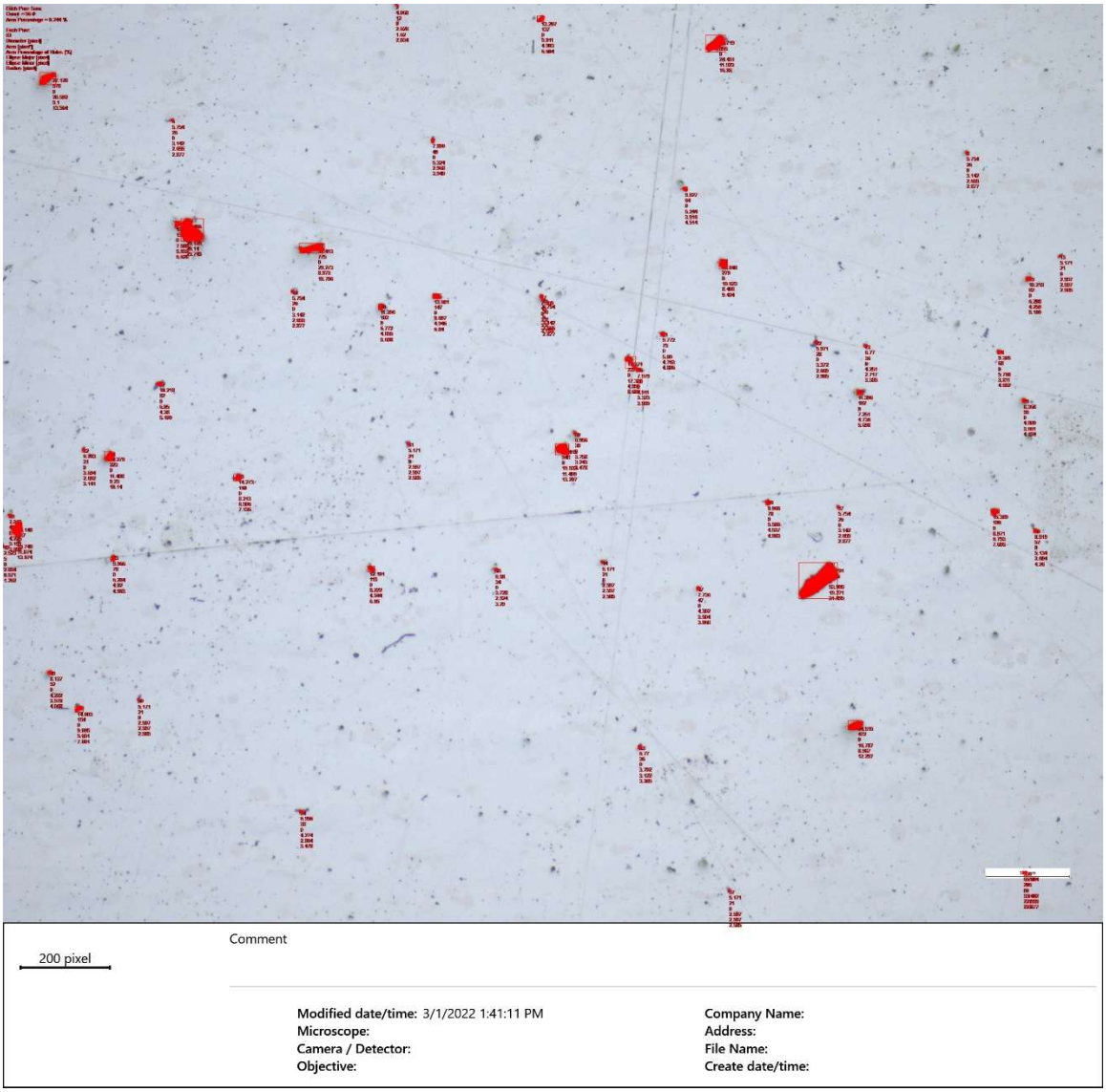

Figure A 4: Sample 5 porosity

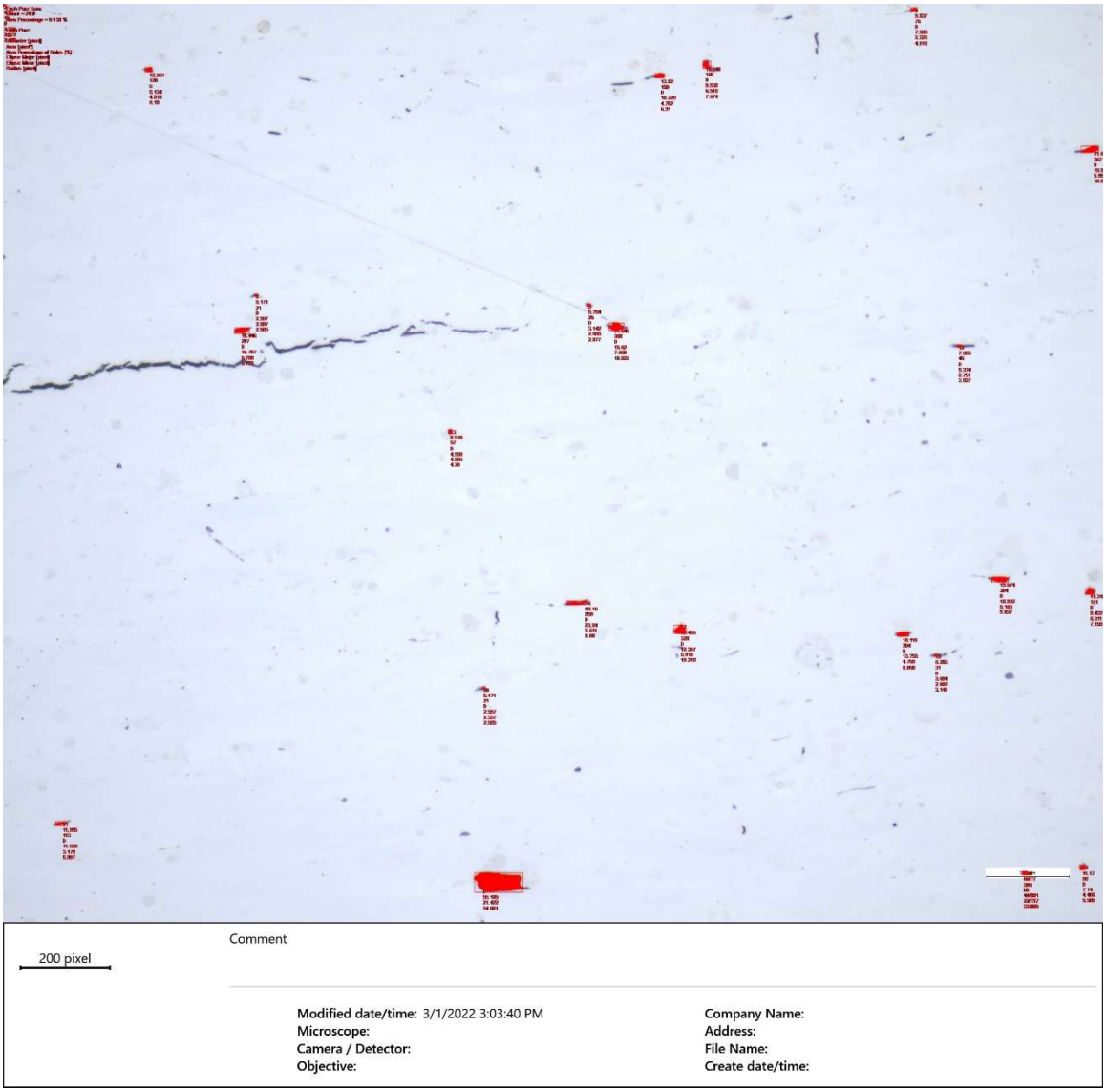

Figure A 5: Sample 5+ porosity

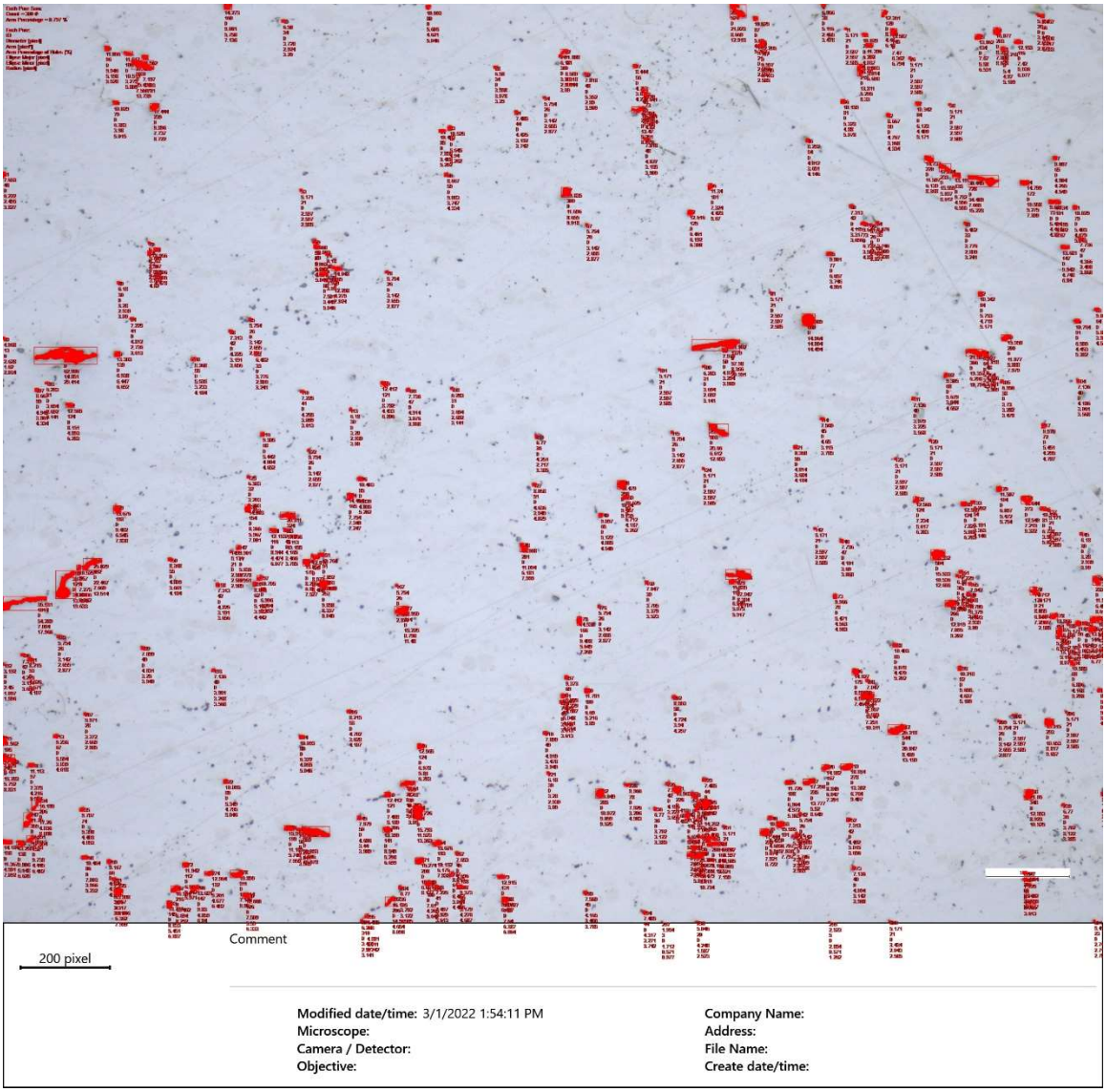

Figure A 6: Sample 7 porosity

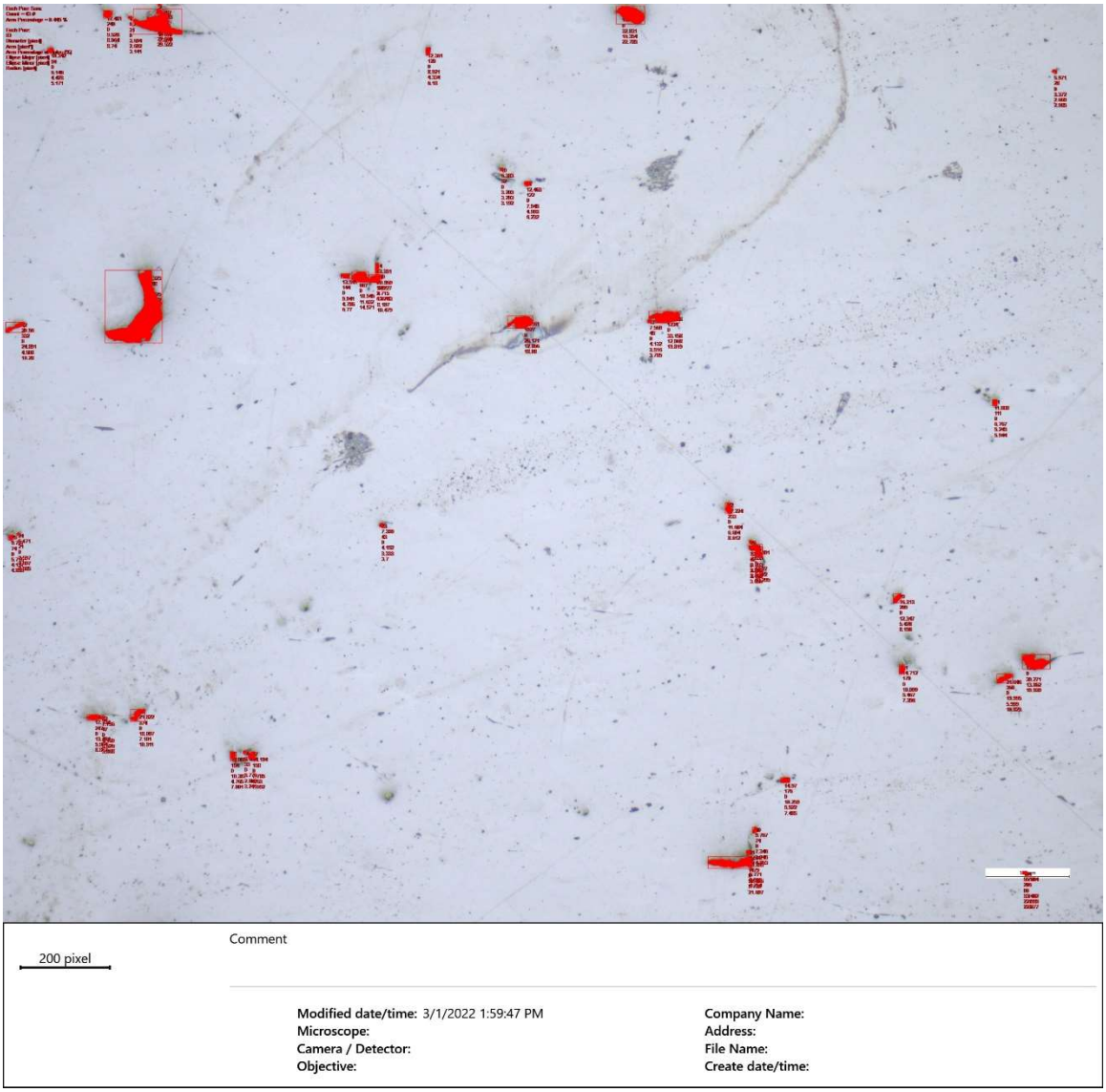

Figure A 7: Sample 7+ porosity

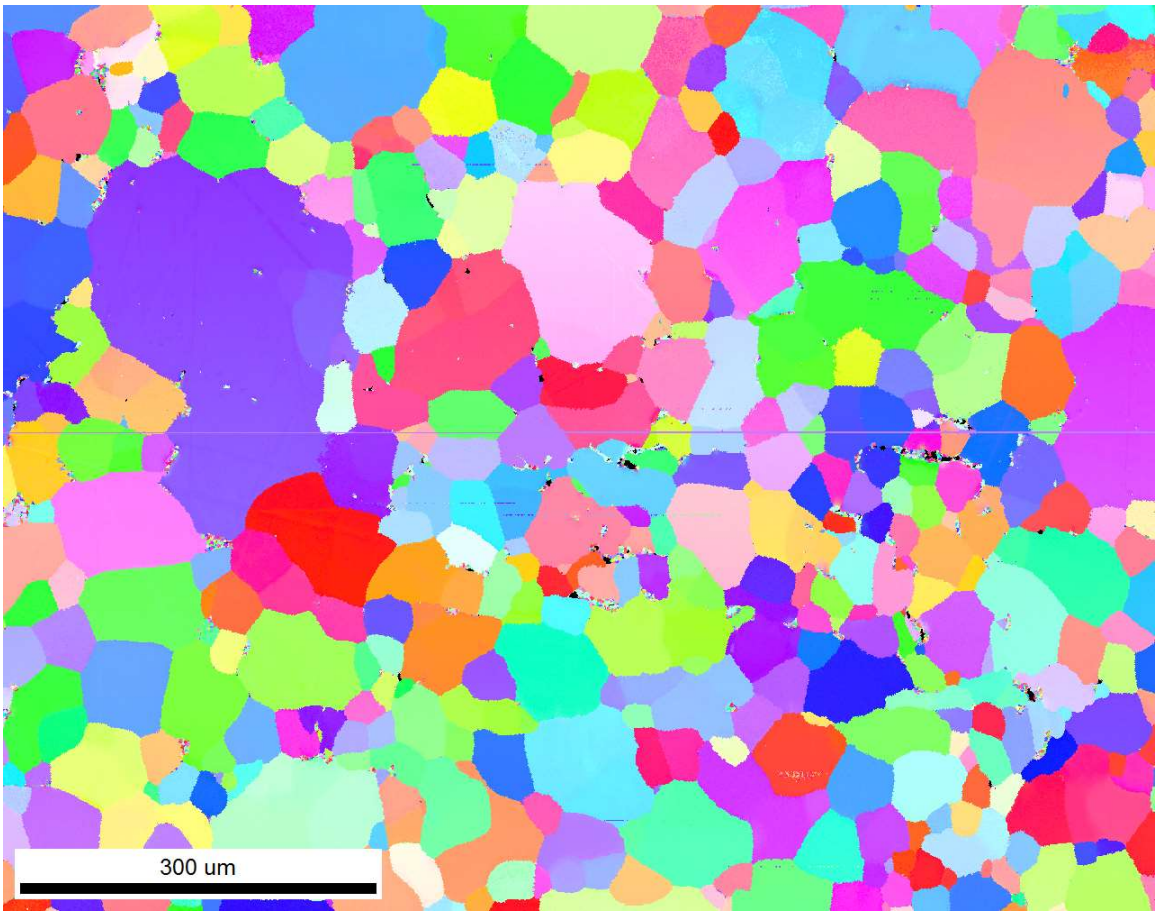

Figure A 8: Sample 2 EBSD 1

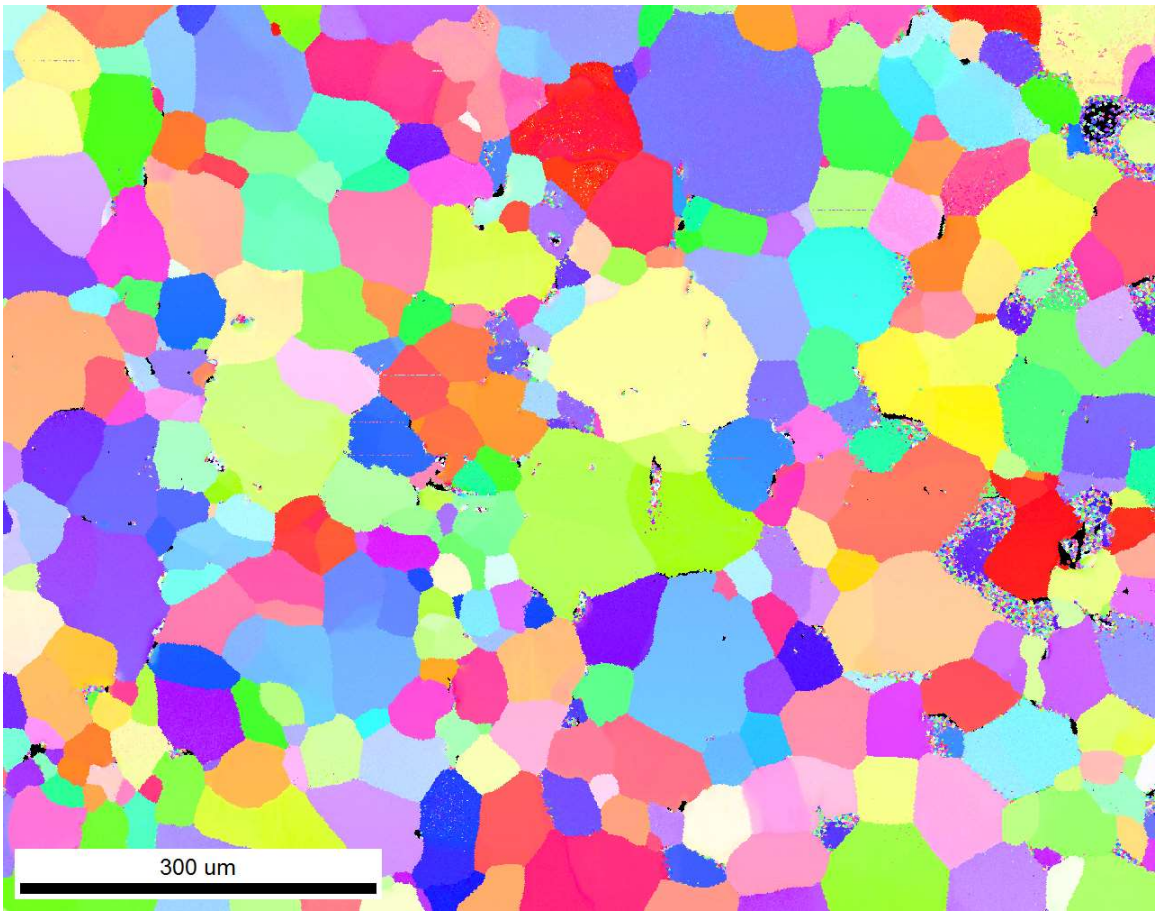

Figure A 9: Sample 2 EBSD 3

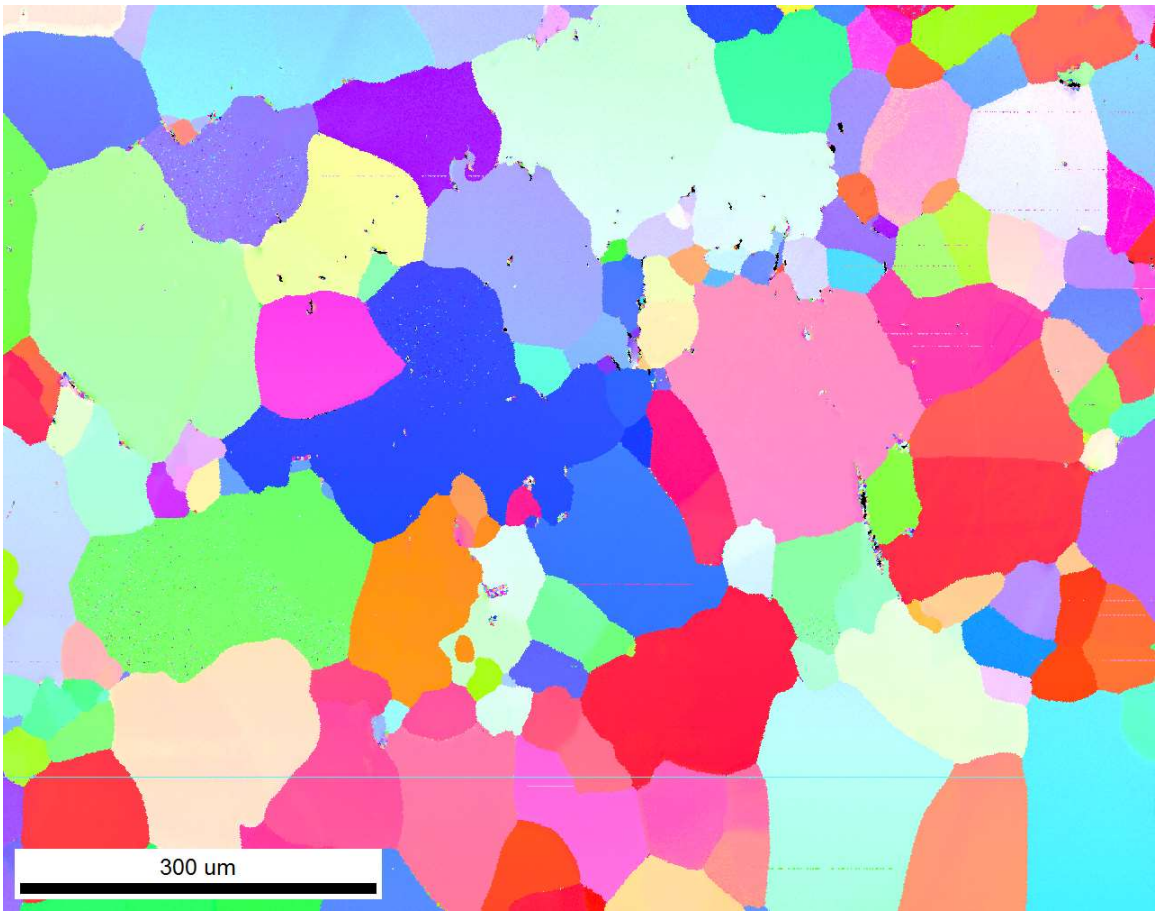

Figure A 10: Sample 3 EBSD 1

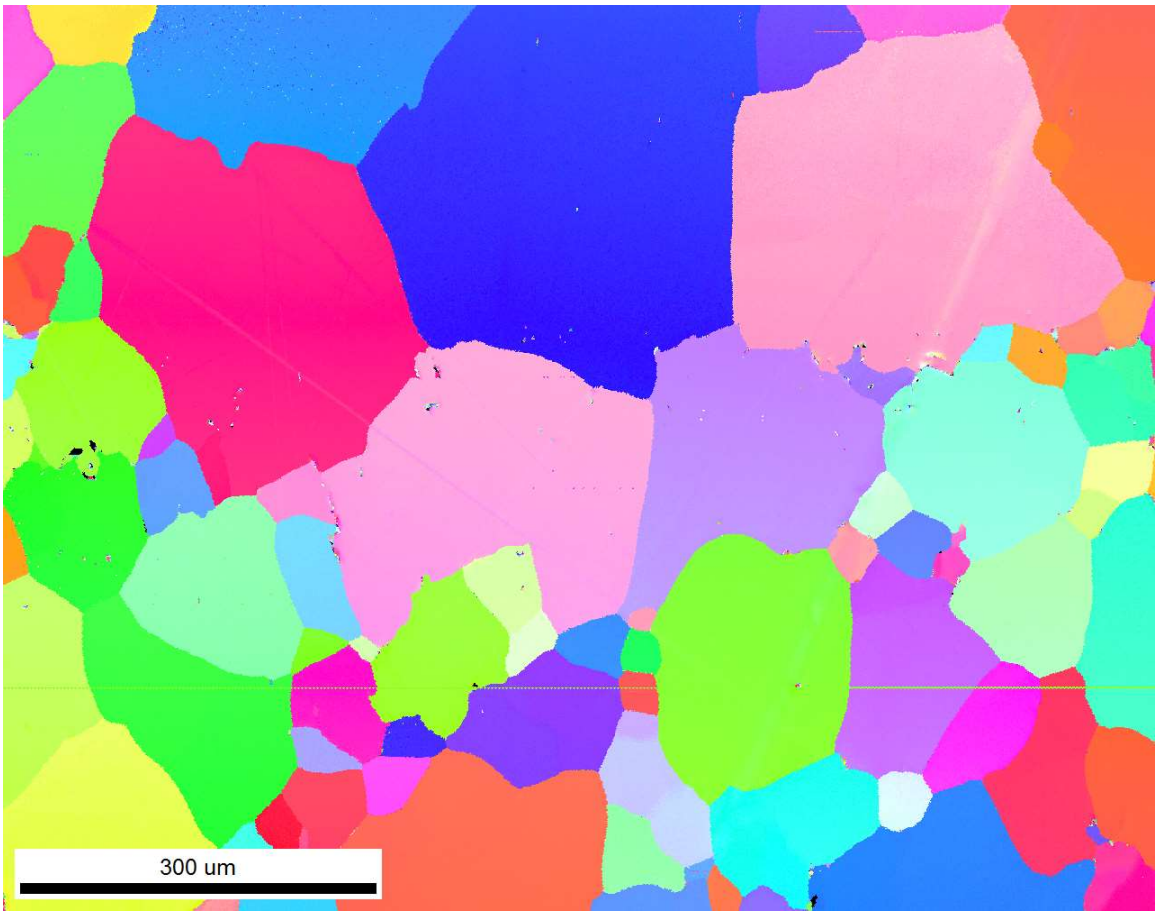

Figure A 11: Sample 3 EBSD 3

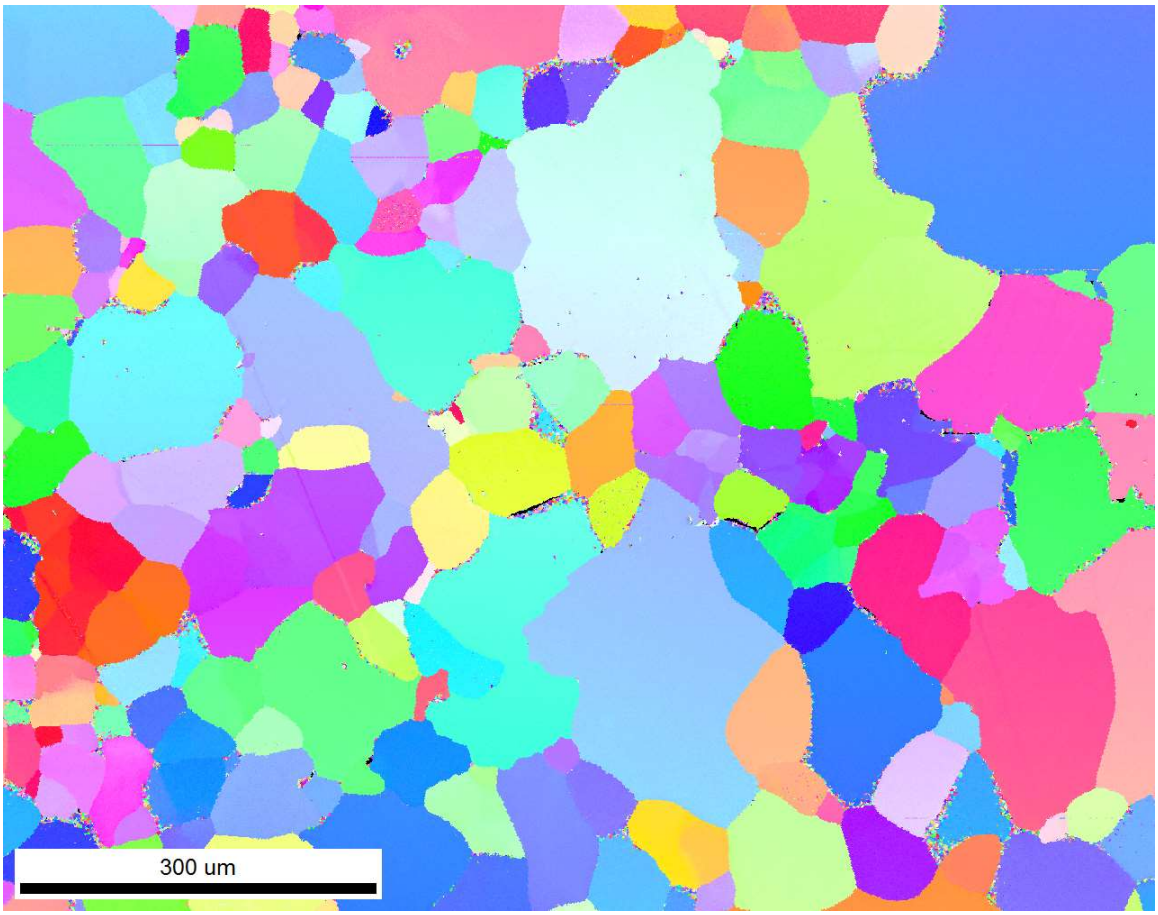

Figure A 12: Sample 5 EBSD 1

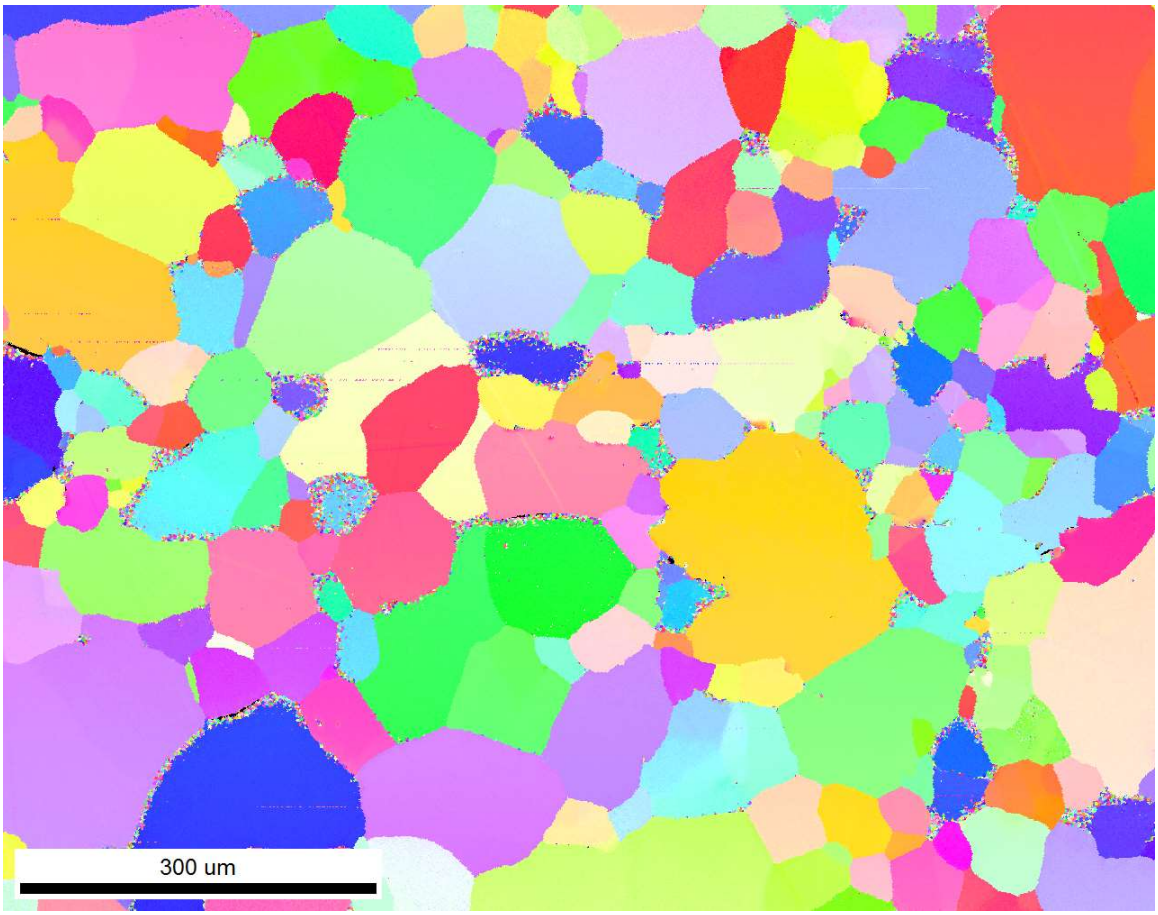

Figure A 13: Sample 5 EBSD 2

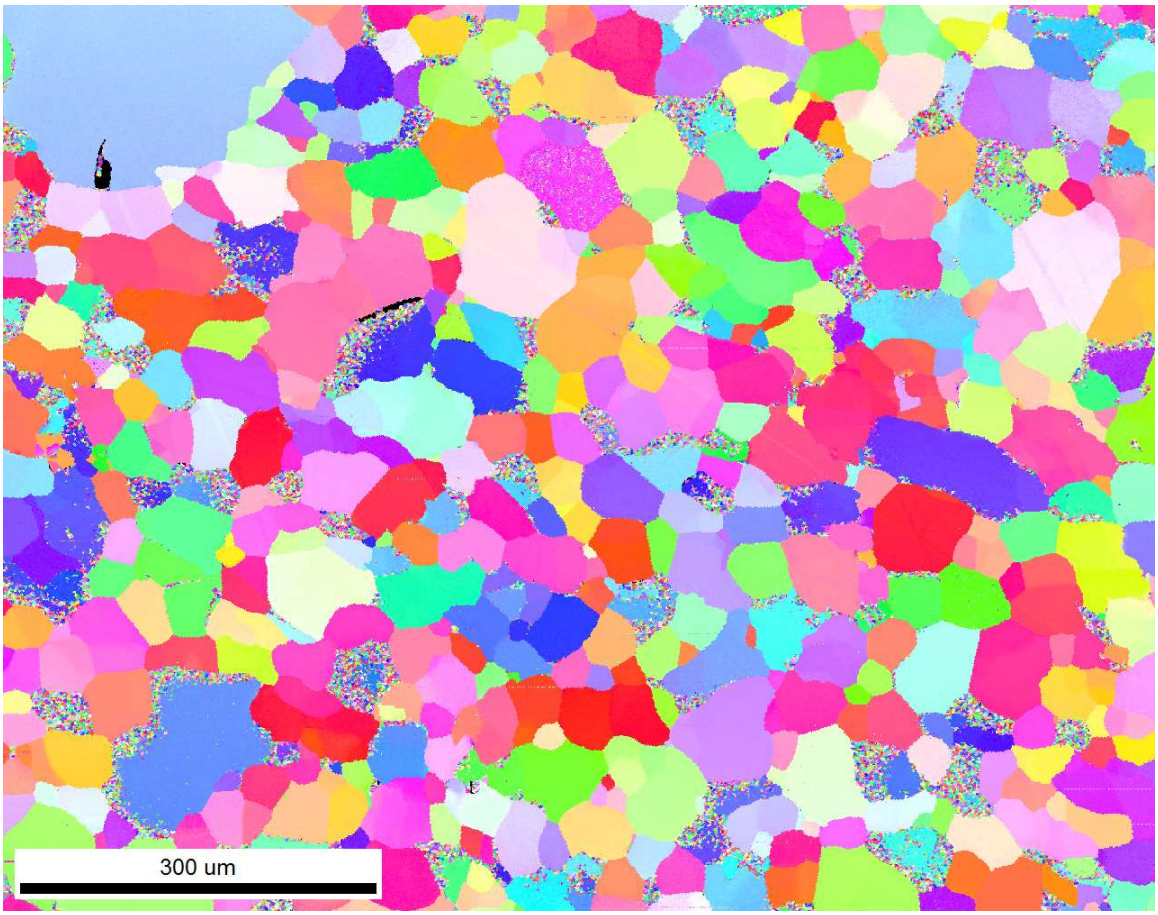

Figure A 14: Sample 7 EBSD 1

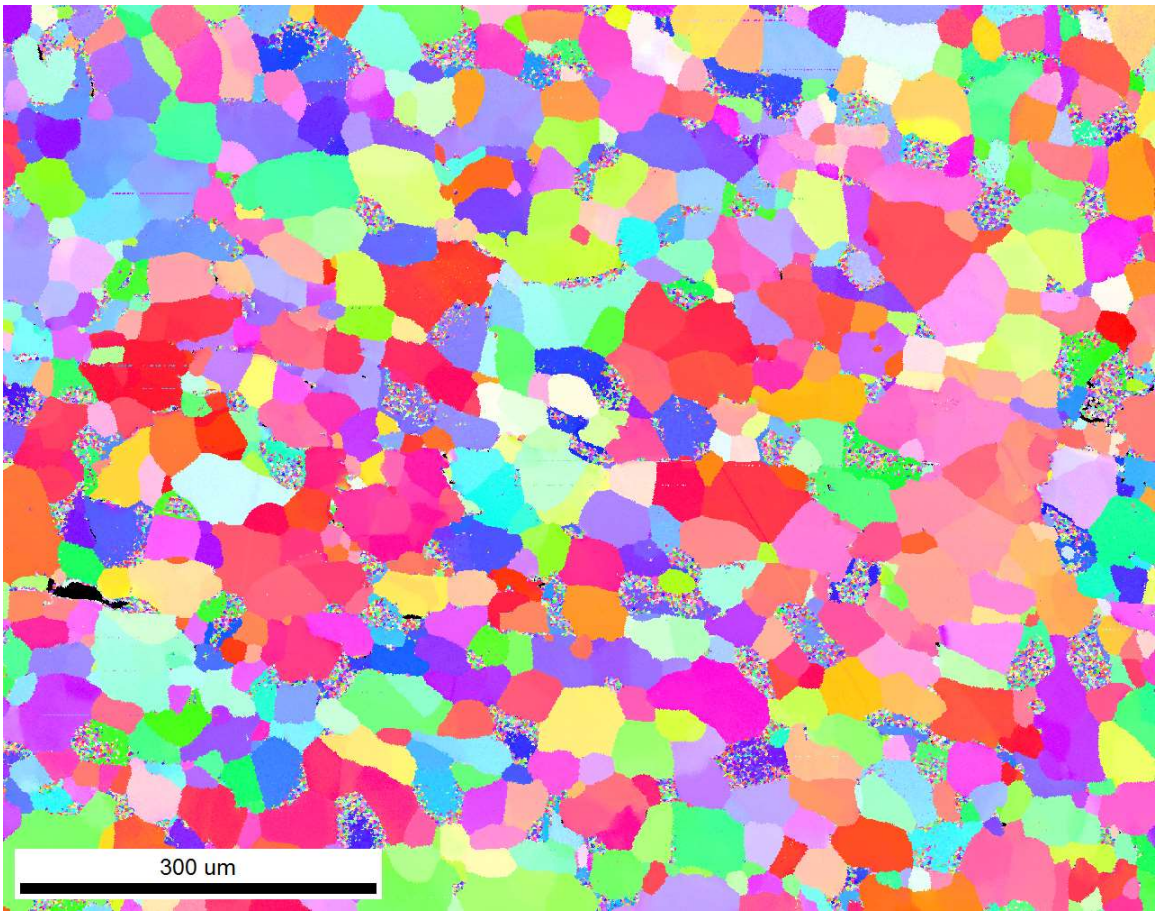

Figure A 15: Sample 7 EBSD 2

RFERENCES

[1] M. L. Bauccio, *ASM Metals Reference Book*, 1st ed. ASM International, 1993.

[2] E. Lassner and W.-D. Schubert, *Tungsten*, 1st ed. Boston, MA: Springer US, 1999. doi: 10.1007/978-1-4615-4907-9.

[3] B. S. Li, T. J. Marrow, and D. E. J. Armstrong, "Measuring the brittle-to-ductile transition temperature of tungsten–tantalum alloy using chevron-notched micro-cantilevers," *Scripta Materialia*, vol. 180, pp. 77–82, Apr. 2020, doi: 10.1016/J.SCRIPTAMAT.2020.01.030.

[4] B. Vrancken, R. K. Ganeriwala, and M. J. Matthews, "Analysis of laser-induced microcracking in tungsten under additive manufacturing conditions: Experiment and simulation," *Acta Materialia*, vol. 194, pp. 464–472, Aug. 2020, doi: 10.1016/J.ACTAMAT.2020.04.060.

[5] J. Xue, Z. Feng, J. Tang, C. Tang, and Z. Zhao, "Selective laser melting additive manufacturing of tungsten with niobium alloying: Microstructure and suppression mechanism of microcracks," *Journal of Alloys and Compounds*, vol. 874, p. 159879, Sep. 2021, doi: 10.1016/J.JALLCOM.2021.159879.

[6] D. Wang, Z. Wang, K. Li, J. Ma, W. Liu, and Z. Shen, "Cracking in laser additively manufactured W: Initiation mechanism and a suppression approach by alloying," *Materials & Design*, vol. 162, pp. 384–393, Jan. 2019, doi: 10.1016/J.MATDES.2018.12.010.

[7] C. Yin *et al.*, "Ductile to brittle transition temperature of advanced tungsten alloys for nuclear fusion applications deduced by miniaturized three-point bending tests," *International Journal of Refractory Metals and Hard Materials*, vol. 95, p. 105464, Feb. 2021, doi: 10.1016/J.IJRMHM.2020.105464.

[8] A. Iveković *et al.*, "Selective laser melting of tungsten and tungsten alloys," *International Journal of Refractory Metals and Hard Materials*, vol. 72, pp. 27–32, Apr. 2018, doi: 10.1016/J.IJRMHM.2017.12.005.

[9] S. Whang, Ed., *Nanostructured Metals and Alloys Processing, Microstructure, Mechanical Properties and Applications*, 1st ed. Woodhead Publishing, 2011.

[10] J. Braun *et al.*, "Molybdenum and tungsten manufactured by selective laser melting: Analysis of defect structure and solidification mechanisms," *International Journal of Refractory Metals and Hard Materials*, vol. 84, p. 104999, Nov. 2019, doi: 10.1016/J.IJRMHM.2019.104999.

[11] C. Tan, K. Zhou, W. Ma, B. Attard, P. Zhang, and T. Kuang, “Selective laser melting of high-performance pure tungsten: parameter design, densification behavior and mechanical properties,” *Science and Technology of Advanced Materials*, vol. 19, no. 1, pp. 370–380, Dec. 2018, doi: 10.1080/14686996.2018.1455154.

[12] D. H. Killefer and A. Linz, *Molybdenum Compounds: Their Chemistry and Technology*, 1st ed. New York: Interscience, 1952.

[13] T. A. Parthasarathy, M. G. Mendiratta, and D. M. Dimiduk, “Oxidation mechanisms in Mo-reinforced Mo5SiB2(T2)–Mo3Si alloys,” *Acta Materialia*, vol. 50, no. 7, pp. 1857–1868, Apr. 2002, doi: 10.1016/S1359-6454(02)00039-3.

[14] A. T. Nelson, E. S. Sooby, Y. J. Kim, B. Cheng, and S. A. Maloy, “High temperature oxidation of molybdenum in water vapor environments,” *Journal of Nuclear Materials*, vol. 448, no. 1–3, pp. 441–447, May 2014, doi: 10.1016/J.JNUCMAT.2013.10.043.

[15] I. Wesemann, A. Hoffmann, T. Mrotzek, and U. Martin, “Investigation of solid solution hardening in molybdenum alloys,” *International Journal of Refractory Metals and Hard Materials*, vol. 28, no. 6, pp. 709–715, Nov. 2010, doi: 10.1016/J.IJRMHM.2010.05.010.

[16] C. Chaopeng, Z. Xiangwei, L. Qiang, Z. Min, Z. Guangping, and L. Shulong, “Study on high temperature strengthening mechanism of ZrO2/Mo alloys,” *Journal of Alloys and Compounds*, vol. 829, p. 154630, Jul. 2020, doi: 10.1016/J.JALLCOM.2020.154630.

[17] D. Wang, C. Yu, J. Ma, W. Liu, and Z. Shen, “Densification and crack suppression in selective laser melting of pure molybdenum,” *Materials & Design*, vol. 129, pp. 44–52, Sep. 2017, doi: 10.1016/J.MATDES.2017.04.094.

[18] L. Kaserer *et al.*, “Microstructure and mechanical properties of molybdenum-titanium-zirconium-carbon alloy TZM processed via laser powder-bed fusion,” *International Journal of Refractory Metals and Hard Materials*, vol. 93, p. 105369, Dec. 2020, doi: 10.1016/J.IJRMHM.2020.105369.

[19] M. Oku, S. Suzuki, H. Kurishita, and H. Yoshinaga, “Chemical states of oxygen segregated intergranular fracture surfaces of molybdenum,” *Applied Surface Science*, vol. 26, no. 1, pp. 42–50, Jun. 1986, doi: 10.1016/0169-4332(86)90051-6.

[20] K. Leitner (née Babinsky) *et al.*, “On grain boundary segregation in molybdenum materials,” *Materials & Design*, vol. 135, pp. 204–212, Dec. 2017, doi: 10.1016/J.MATDES.2017.09.019.

[21] K. Leitner (née Babinsky) *et al.*, “Grain boundary segregation engineering in as-sintered molybdenum for improved ductility,” *Scripta Materialia*, vol. 156, pp. 60–63, Nov. 2018, doi: 10.1016/J.SCRIPTAMAT.2018.07.008.

[22] J. B. Brosse, R. Fillit, and M. Biscondi, “Intrinsic intergranular brittleness of molybdenum,” *Scripta Metallurgica*, vol. 15, no. 6, pp. 619–623, Jun. 1981, doi: 10.1016/0036-9748(81)90038-7.

[23] K. Babinsky, J. Weidow, W. Knabl, A. Lorich, H. Leitner, and S. Primig, “Atom probe study of grain boundary segregation in technically pure molybdenum,” *Materials Characterization*, vol. 87, pp. 95–103, Jan. 2014, doi: 10.1016/J.MATCHAR.2013.11.001.

[24] M. Winter, *Re Organorhenium Compounds*. Berlin, Heidelberg: Springer Berlin Heidelberg, 1988. doi: 10.1007/978-3-662-08844-9.

[25] T. Leonhardt, J.-C. Carlén, M. Buck, C. R. Brinkman, W. Ren, and C. O. Stevens, “Investigation of mechanical properties and microstructure of various molybdenum-rhenium alloys,” *AIP Conference Proceedings*, vol. 458, no. 1, pp. 685–690, Jan. 1999, doi: 10.1063/1.57638.

[26] S. R. Agnew and T. Leonhardt, “The low-temperature mechanical behavior of molybdenum-rhenium,” *JOM*, vol. 55, no. 10, pp. 25–29, 2003, doi: 10.1007/s11837-003-0171-2.

[27] M. J. Witcomb, “Oxidation of thin molybdenum-rhenium foils,” *Journal of the Less Common Metals*, vol. 41, no. 1, pp. 45–57, Jun. 1975, doi: 10.1016/0022-5088(75)90092-2.

[28] C. C. Eckley, R. A. Kemnitz, C. P. Fassio, C. R. Hartsfield, and T. A. Leonhardt, “Selective Laser Melting of Tungsten-Rhenium Alloys,” *JOM*, vol. 73, no. 11, pp. 3439–3450, 2021, doi: 10.1007/s11837-021-04776-x.

[29] W. D. Klopp, F. C. Holden, and R. I. Jaffee, “FURTHER STUDIES ON RHENIUM ALLOYING EFFECTS IN MOLYBDENUM, TUNGSTEN, AND CHROMIUM,” United States, 1960. [Online]. Available: https://www.osti.gov/biblio/4138854

[30] W. D. Klopp and W. R. Witzke, “MECHANICAL PROPERTIES OF ELECTRON-BEAM-MELTED MOLYBDENUM AND DILUTE MOLYBDENUM--RHENIUM ALLOYS.,” Country unknown/Code not available, 1972. [Online]. Available: https://www.osti.gov/biblio/4608252

[31] R. I. Jaffee and C. T. Sims, “THE EFFECT OF RHENIUM ON THE FABRICABILITY AND DUCTILITY OF MOLYBDENUM AND TUNGSTEN,” United States, 1958. [Online]. Available: https://www.osti.gov/biblio/4342529

[32] P. L. Raffo, “Yielding and fracture in tungsten and tungsten-rhenium alloys,” *Journal of the Less Common Metals*, vol. 17, no. 2, pp. 133–149, Feb. 1969, doi: 10.1016/0022-5088(69)90047-2.

[33] J. R. Stephens and W. R. Witzke, “Alloy hardening and softening in binary molybdenum alloys as related to electron concentration,” *Journal of the Less Common Metals*, vol. 29, no. 4, pp. 371–388, Dec. 1972, doi: 10.1016/0022-5088(72)90201-9.

[34] L. Xu, S. Wei, J. Li, G. Zhang, and B. Dai, “Preparation, microstructure and properties of molybdenum alloys reinforced by in-situ Al2O3 particles,” *International Journal of Refractory Metals and Hard Materials*, vol. 30, no. 1, pp. 208–212, Jan. 2012, doi: 10.1016/J.IJRMHM.2011.08.012.

[35] L. Xu, T. Sun, Y. Zhou, F. Xiao, M. Zhang, and S. Wei, “Evaluating compressive property and hot deformation behavior of molybdenum alloy reinforced by nanoscale zirconia particles,” *Journal of Alloys and Compounds*, vol. 860, p. 158289, Apr. 2021, doi: 10.1016/J.JALLCOM.2020.158289.

[36] F. Xiao *et al.*, “Extremely uniform nanosized oxide particles dispersion strengthened tungsten alloy with high tensile and compressive strengths fabricated involving liquid-liquid method,” *Journal of Alloys and Compounds*, vol. 878, p. 160335, Oct. 2021, doi: 10.1016/J.JALLCOM.2021.160335.

[37] J. Wadsworth, “A reevaluation of the mechanical properties of molybdenum- and tungsten-based alloys containing hafnium and carbon,” *Metallurgical Transactions A*, vol. 14, no. 1, pp. 285–294, 1983, doi: 10.1007/BF02651625.

[38] X. S. Liu *et al.*, “Investigations on microstructure and mechanical properties of HfC particle-reinforced WMo composites,” *International Journal of Refractory Metals and Hard Materials*, vol. 100, p. 105634, Nov. 2021, doi: 10.1016/J.IJRMHM.2021.105634.

[39] J. Braun, L. Kaserer, I. Letofsky-Papst, K. H. Leitz, H. Kestler, and G. Leichtfried, "On the role of carbon in molybdenum manufactured by Laser Powder Bed Fusion," *International Journal of Refractory Metals and Hard Materials*, vol. 92, p. 105283, Nov. 2020, doi: 10.1016/J.IJRMHM.2020.105283.

[40] L. Kaserer *et al.*, "Fully dense and crack free molybdenum manufactured by Selective Laser Melting through alloying with carbon," *International Journal of Refractory Metals and Hard Materials*, vol. 84, p. 105000, Nov. 2019, doi: 10.1016/J.IJRMHM.2019.105000.

[41] K. Leitner *et al.*, "How grain boundary chemistry controls the fracture mode of molybdenum," *Materials & Design*, vol. 142, pp. 36–43, Mar. 2018, doi: 10.1016/J.MATDES.2018.01.012.

[42] J. H. Schneibel, E. J. Felderman, and E. K. Ohriner, "Mechanical properties of ternary molybdenum–rhenium alloys at room temperature and 1700 K," *Scripta Materialia*, vol. 59, no. 2, pp. 131–134, Jul. 2008, doi: 10.1016/J.SCRIPTAMAT.2008.02.057.

[43] J. Dong *et al.*, "Effect of atmosphere on the microstructure and properties of additively manufactured tungsten," *Materials Science and Technology*, vol. 36, no. 18, pp. 1988–1996, Dec. 2020, doi: 10.1080/02670836.2020.1852680.

[44] A. C. Field, L. N. Carter, N. J. E. Adkins, M. M. Attallah, M. J. Gorley, and M. Strangwood, "The Effect of Powder Characteristics on Build Quality of High-Purity Tungsten Produced via Laser Powder Bed Fusion (LPBF)," *Metallurgical and Materials Transactions A*, vol. 51, no. 3, pp. 1367–1378, 2020, doi: 10.1007/s11661-019-05601-6.

[45] F. Ahmed *et al.*, "Study of powder recycling and its effect on printed parts during laser powder-bed fusion of 17-4 PH stainless steel," *Journal of Materials Processing Technology*, vol. 278, p. 116522, Apr. 2020, doi: 10.1016/J.JMATPROTEC.2019.116522.

[46] F. Yi, Q. Zhou, C. Wang, Z. Yan, and B. Liu, "Effect of powder reuse on powder characteristics and properties of Inconel 718 parts produced by selective laser melting," *Journal of Materials Research and Technology*, vol. 13, pp. 524–533, Jul. 2021, doi: 10.1016/J.JMRT.2021.04.091.

[47] N. E. Gorji, R. O'Connor, A. Mussatto, M. Snelgrove, P. G. M. González, and D. Brabazon, "Recyclability of stainless steel (316 L) powder within the additive

manufacturing process," *Materialia (Oxf)*, vol. 8, p. 100489, Dec. 2019, doi: 10.1016/J.MTLA.2019.100489.

[48] M. Guo *et al.*, "Selective laser melting additive manufacturing of pure tungsten: Role of volumetric energy density on densification, microstructure and mechanical properties," *International Journal of Refractory Metals and Hard Materials*, vol. 84, p. 105025, Nov. 2019, doi: 10.1016/J.IJRMHM.2019.105025.

[49] D. Faidel, D. Jonas, G. Natour, and W. Behr, "Investigation of the selective laser melting process with molybdenum powder," *Additive Manufacturing*, vol. 8, pp. 88–94, Oct. 2015, doi: 10.1016/J.ADDMA.2015.09.002.

[50] M. Higashi and T. Ozaki, "Selective laser melting of pure molybdenum: Evolution of defect and crystallographic texture with process parameters," *Materials & Design*, vol. 191, p. 108588, Jun. 2020, doi: 10.1016/J.MATDES.2020.108588.

[51] P. Fernandez-Zelaia *et al.*, "Crystallographic texture evolution in electron beam melting additive manufacturing of pure Molybdenum," *Materials & Design*, vol. 207, p. 109809, Sep. 2021, doi: 10.1016/J.MATDES.2021.109809.

[52] X. Zhou, X. Liu, D. Zhang, Z. Shen, and W. Liu, "Balling phenomena in selective laser melted tungsten," *Journal of Materials Processing Technology*, vol. 222, pp. 33–42, Aug. 2015, doi: 10.1016/J.JMATPROTEC.2015.02.032.

[53] X. Zhou, X. Liu, D. Zhang, Z. Shen, and W. Liu, "Balling phenomena in selective laser melted tungsten," *Journal of Materials Processing Technology*, vol. 222, pp. 33–42, Aug. 2015, doi: 10.1016/J.JMATPROTEC.2015.02.032.

[54] J. Li, Y. Wu, B. Zhou, and Z. Wei, "Laser Powder Bed Fusion of Pure Tungsten: Effects of Process Parameters on Morphology, Densification, Microstructure," *Materials*, vol. 14, no. 1, 2021, doi: 10.3390/ma14010165.

[55] B. Vrancken, R. K. Ganeriwala, A. A. Martin, and M. J. Matthews, "Microcrack mitigation during laser scanning of tungsten via preheating and alloying strategies," *Additive Manufacturing*, vol. 46, p. 102158, Oct. 2021, doi: 10.1016/J.ADDMA.2021.102158.

[56] T. Shen, Y. Dai, and Y. Lee, "Microstructure and tensile properties of tungsten at elevated temperatures," *Journal of Nuclear Materials*, vol. 468, pp. 348–354, Jan. 2016, doi: 10.1016/J.JNUCMAT.2015.09.057.

[57] B. v. Cockeram, "The role of stress state on the fracture toughness and toughening mechanisms of wrought molybdenum and molybdenum alloys," *Materials Science*

and Engineering: A, vol. 528, no. 1, pp. 288–308, Nov. 2010, doi: 10.1016/J.MSEA.2010.09.009.

[58] T. Watanabe and S. Tsurekawa, "The control of brittleness and development of desirable mechanical properties in polycrystalline systems by grain boundary engineering," *Acta Materialia*, vol. 47, no. 15–16, pp. 4171–4185, Nov. 1999, doi: 10.1016/S1359-6454(99)00275-X.

[59] Y. Zhou, L. Duan, F. Li, K. Chen, and S. Wen, "Effect of heat treatment on the microstructure and mechanical property of W/316L multi-material fabricated by selective laser melting," *Journal of Alloys and Compounds*, vol. 890, p. 161841, Jan. 2022, doi: 10.1016/J.JALLCOM.2021.161841.

[60] G. Faraji, H. S. Kim, and H. T. Kashi, "Chapter 6 - Effective Parameters for the Success of Severe Plastic Deformation Methods," in *Severe Plastic Deformation*, G. Faraji, H. S. Kim, and H. T. Kashi, Eds. Elsevier, 2018, pp. 187–222. doi: https://doi.org/10.1016/B978-0-12-813518-1.00006-0.

[61] R. Ohser-Wiedemann, U. Martin, A. Müller, and G. Schreiber, "Spark plasma sintering of Mo–W powders prepared by mechanical alloying," *Journal of Alloys and Compounds*, vol. 560, pp. 27–32, May 2013, doi: 10.1016/J.JALLCOM.2013.01.142.